NASA/TP-20250006708

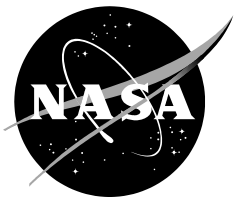

# Development of the NASA HR-2 Superalloy for Hydrogen-Sensitive Liquid Rocket Engines Via Laser Powder Bed Fusion

*Po-Shou Chen[1], Benjamin L. Rupp[2], Colton S. Katsarelis[2], Ching Hua Su[2], Diana Y. Andreev[1], and Abram G. Culver[1]*

*[1]Amentum ESSCA Group, Huntsville, Alabama*
*[2]Marshall Space Flight Center, Huntsville, Alabama*

# NASA STI Program Report Series

The NASA STI Program collects, organizes, provides for archiving, and disseminates NASA's STI. The NASA STI Program provides access to the NTRS Registered and its public interface, the NASA Technical Reports Server, thus providing one of the largest collections of aeronautical and space science STI in the world. Results are published in both non-NASA channels and by NASA in the NASA STI Report Series, which includes the following report types:

- TECHNICAL PUBLICATION. Reports of completed research or a major significant phase of research that present the results of NASA Programs and include extensive data or theoretical analysis. Includes compilations of significant scientific and technical data and information deemed to be of continuing reference value. NASA counterpart of peer-reviewed formal professional papers but has less stringent limitations on manuscript length and extent of graphic presentations.

- TECHNICAL MEMORANDUM. Scientific and technical findings that are preliminary or of specialized interest, e.g., quick release reports, working papers, and bibliographies that contain minimal annotation. Does not contain extensive analysis.

- CONTRACTOR REPORT. Scientific and technical findings by NASA-sponsored contractors and grantees.

- CONFERENCE PUBLICATION. Collected papers from scientific and technical conferences, symposia, seminars, or other meetings sponsored or co-sponsored by NASA.

- SPECIAL PUBLICATION. Scientific, technical, or historical information from NASA programs, projects, and missions, often concerned with subjects having substantial public interest.

- TECHNICAL TRANSLATION. English-language translations of foreign scientific and technical material pertinent to NASA's mission.

Specialized services also include organizing and publishing research results, distributing specialized research announcements and feeds, providing information desk and personal search support, and enabling data exchange services.

For more information about the NASA STI Program, see the following:

- Access the NASA STI Program home page at http://www.sti.nasa.gov

NASA/TP-20250006708

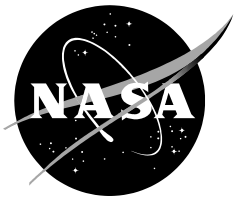

# Development of the NASA HR-2 Superalloy for Hydrogen-Sensitive Liquid Rocket Engines Via Laser Powder Bed Fusion

*Po-Shou Chen[1], Benjamin L. Rupp[2], Colton S. Katsarelis[2], Ching Hua Su[2], Diana Y. Andreev[1], and Abram G. Culver[1]*

*[1]Amentum ESSCA Group, Huntsville, Alabama*
*[2]Marshall Space Flight Center, Huntsville, Alabama*

National Aeronautics and
Space Administration

*Marshall Space Flight Center*
*Huntsville, Alabama*

**July 2025**

## Acknowledgments

The authors would like to acknowledge the mechanical test team that includes Keith Hastings, Jacob Faulk, Matthew Jackson, and Allisson Peusch. These team members performed tensile tests in a 5-ksi high-pressure gaseous hydrogen environment, in cryogenic conditions, and at elevated temperatures. Tensile property data were provided in a timely fashion to allow for clear and decisive direction on the development of L-PBF NASA HR-2.

The authors also acknowledge the powder quality analysis work of Justin McElderry and surface quality analysis work of Matthew Mazurkivich.

# Table of Contents

**List of Figures**

**List of Tables**

**Acronyms**

| | |
|---|---|
| Al | aluminum |
| AM | additive manufacturing |
| Ar | argon |
| B | boron |
| BD | build direction |
| C | carbon |
| Co | cobalt |
| Cr | chromium |
| DSC | differential scanning calirimetry |
| FCC | face-centered cubic |
| H | hydrogen |
| HAZ | heat-affected zone |
| HCF | high cycle fatigue |
| HEE | hydrogen environment embrittlement |
| HIP | hot isostatic pressing |
| HR | hydrogen-resistant |
| HTF | Hydrogen Test Facility |
| Fe | iron |
| $GH_2$ | gaseous hydrogen |
| LCF | low cycle fatigue |
| L-PBF | laser-powder bed fusion |
| LPFTP | low-pressure fuel turbopump |
| LRE | liquid rocket engine |
| LSG | low stress grinding |
| NASA | National Aeronautics and Space Administration |
| Mn | manganese |

| | |
|---|---|
| Mo | molybdenum |
| MSFC | Marshall Space Flight Center |
| N | nitrogen |
| Ni | nickel |
| O | oxygen |
| P | phosphorus |
| PAC | Powder Alloy Corporation |
| PHACOMP | PHAse COMPutation |
| Ra | surface roughness |
| S | sulfur |
| Si | silicon |
| SEM | scanning electron microscopy |
| SFE | stacking fault energy |
| STR | solidification temperature range |
| TC | test cell |
| TD | transverse direction |
| Ti | titanium |
| Tm | melting temperature |
| UTS | ultimate tensile strength or ultimate tensile stress |
| V | vanadium |
| W | tungsten |
| YS | yield strength |

## 1.0 Introduction

The National Aeronautics and Space Administration (NASA) has played a leading role in advancing metal additive manufacturing (AM) for space applications since the late 2000s. AM has provided new design and manufacturing opportunities to reduce cost and schedule, consolidate parts, and optimize performance. Conventional production of high-performance metallic parts requires a costly and tedious manufacturing route that involves vacuum induction melting and vacuum arc melting, followed by hot- or cold-rolling or forging and machining to fabricate individual parts. In comparison, AM has demonstrated a schedule savings of 2–10x over these traditional methods and a cost reduction on the order of 50% or greater **[1]**. As such, AM has matured rapidly for use in propulsion systems, for many components in both flight and developmental applications.

Mechanical property degradation of materials due to hydrogen environment embrittlement (HEE) from exposure to high-pressure gaseous hydrogen ($GH_2$) is a critical concern in liquid hydrogen ($LH_2$) propulsion systems **[2, 3]**. In light of this issue and the advantages of AM, NASA has identified the need to develop and advance new AM-optimized materials for use in the unique application of liquid rocket engines (LREs) using $LH_2$ as a propellant **[1, 4–8]**.

One such material being developed at MSFC is laser-powder bed fusion (L-PBF) NASA Hydrogen Resistant-2 (HR-2). NASA HR-2 is a HEE-resistant, nickel-iron (Ni-Fe)-based, γ′-strengthened superalloy alloyed with cobalt (Co), chromium (Cr), molybdenum (Mo), tungsten (W), titanium (Ti), and aluminum (Al) for high strength and ductility. NASA HR-2 was derived from NASA HR-1 **[2, 7]** to increase strength and enhance microstructure evolution from an as-built arc-shaped coarse structure to a fine equiaxed grain structure after post-processing heat treatment. The alloy development was approached by formulating a hydrogen-resistant $\gamma$ matrix that resembles NASA HR-1 along with increasing strength by promoting γ′ precipitation and solid-solution strengthening of the γ matrix.

L-PBF is an AM process that uses a laser to selectively fuse powder in a bed, enabling the production of complex, high-resolution components. Its precision, combined with potential cost and schedule advantages over traditional manufacturing, makes it a promising process for NASA HR-2 to serve as an affordable, HEE-resistant AM alloy for LRE applications.

Due to the strong resistance to HEE, alloys A-286 and JBK-75 are used in the RS-25 engine for hydrogen-sensitive components. However, both alloys have significant limitations as they cannot be readily built using L-PBF. A-286 is very difficult to weld as it is highly susceptible to fusion zone hot cracking and heat-affected zone (HAZ) micro-fissuring **[9]**. JBK-75 is more weldable than A-286, but it is susceptible to hot cracking during L-PBF **[10]**. To address these issues, NASA HR-2 was specifically developed as a solution for fabricating hydrogen-sensitive LRE components via L-PBF. The development of L-PBF NASA HR-2 has advanced through process development using various L-PBF process parameters to assess their effect on defect formation, microstructure evolution, and process economics. L-PBF NASA HR-2 has undergone in-depth metallurgical evaluations, heat treatment studies, detailed microstructure characterization, and mechanical testing across a broad range of temperatures.

To date, the L-PBF NASA HR-2 alloy has demonstrated its excellent printability and strong potential for fabricating complex components in LRE applications requiring high resistance to HEE. Tensile testing performed in a 5-ksi $GH_2$ environment confirmed that hydrogen has little influence on its ductility, strength, and fracture behavior. L-PBF NASA HR-2 is a promising AM alloy for fabrication of hydrogen-sensitive LRE components that require exceptional resistance to HEE. There were many observations and lessons learned from the development of L-PBF NASA HR-2. This paper details the development work completed for L-PBF NASA HR-2, including formulation, L-PBF build processes, heat treatment, microstructure characterization, and mechanical testing. The influence of process parameters on L-PBF printability and densification levels was explored and compared. The latest advancement of the NASA HR-2 alloy in the L-PBF process maturity and LRE hardware development are also discussed. This work was funded under the grants provided by Jacobs' TIPI program and the Liquid Engine Office at Marshall Space Flight Center (MSFC).

## 2. Alloy Chemistry Formulation

NASA HR-2 is a $\gamma'$-strengthened Ni-Fe-based superalloy derived from NASA HR-1 **[2, 7]** to increase strength and improve microstructure evolution after post-processing heat treatment. The alloy design strategy of L-PBF NASA HR-2 was approached by formulating a hydrogen-resistant γ matrix that resembles NASA HR-1 along with increasing γ′ volume fraction and solid-solution strengthening the γ matrix. γ matrix is the primary face-centered cubic (FCC) phase on the Ni lattice that contains significant amounts of elements like Fe, Cr, Co, Mo, and W. PHACOMP (PHAse COMPutation) **[11–16]** was used for L-PBF NASA HR-2 development to ensure stability of the γ matrix and prevent formation of the deleterious η phase ($Ni_3Ti$) at grain boundaries. PHACOMP uses a parameter, *Md*, which is the average d-electron energy above the Fermi energy level of alloying elements in the alloy to estimate the solid solubility of FCC γ matrix.

Overall, the alloy chemistry optimization for L-LBF NASA HR-2 follows the following criteria:

- *Md* level was kept close to that of NASA HR-1 to maintain stability of the γ matrix that is essential to mitigate η-phase formation at grain boundaries.

- Ni and Fe form the matrix of FCC γ phase, which acts as base or solvent for other elements in the alloy. The Ni:Fe ratio was increased slightly to depress *Md* level and improve solid solubility of the matrix γ phase.

- W is an important refractory element that provides persistent solid solution strengthening at elevated temperatures. W was increased to 3.2% to reduce the stacking fault energy (SFE) of the alloy. Lowering the SFE has been shown to decrease the susceptibility to hydrogen embrittlement for several transition metal alloys **[17]**. Another benefit of increasing W content is that the degree of recrystallization after heat treatment increases due to reduction in the SFE **[18]**.

- Similar to W, Mo is also a refractory element that provides persistent solid solution strengthening at elevated temperatures. Mo is also very effective in lowering the SFE for superalloys. Therefore, Mo content was increased up to 3.0% to enhance solid solution strengthening and microstructure evolution after post L-PBF heat treatment.

- Ti and Al are the primary strengthening elements in Ni-Fe-based superalloys as they combine with Ni to form the strengthening γ′ precipitate ($Ni_3$(Ti, Al)). Ti content was increased to 2.8% to obtain an optimal balance of strength and ductility.

PHACOMP can determine a critical *Md* value, above which microstructure instability occurs. For a Ni-Fe-based superalloy, the average value of *Md* can be calculated using equation (1) as shown below.

$$Md = \sum_{i=1}^{n} \text{Xi } (Md)\text{i} \quad (1)$$

Where:

*Md* = average *Md* parameter

Xi = the atomic fraction of the element i in the γ matrix

n = the number of elements in the alloy

(*Md*)i = the *Md* value for element i

The summation is taken over all the alloying elements, i=1, 2…n. When *Md* increases beyond a critical value, the PHACOMP method assumes that the phase instability will occur and that a secondary phase will appear in a terminal solid solution. In other words, the critical *Md* determines the solubility limit of γ matrix. *Md* calculations were performed for NASA HR-2 to yield the *Md* values for two trial chemical compositions, hereafter referred to as "formulation I" and "formulation II."

The critical *Md* value that must be kept below to avoid η-phase formation for LP-DED NASA HR-1 is around 0.9134 **[7]**. Therefore, the *Md* values for L-PBF NASA HR-2 was kept very close to 0.9134 to improve the γ matrix stability and mitigate precipitation of η-phase. An important consideration for the L-PBF NASA HR-2 composition formulation is that its excellent HEE resistance should not be altered. Based on the above approaches, the chemical composition for L-PBF NASA HR-2 was formulated as shown in **Table 1**. **Figure 1** compares the *Md* values for the alloys listed in **Table 1**. Maintaining the *Md* value very close to that of LP-DED NASA HR-1 is intended to mitigate precipitation of the undesirable grain boundary η-phase and enhance HEE resistance. In addition, higher W content in NASA HR-2 formulation II (than that in NASA HR-1) can retard the metastable γ′ to stable η-phase transformation during aging treatment by decreasing the diffusivity of Ti atoms or by increasing the formation of stacking faults **[2].**

**Table 1.** Nominal chemical composition (wt%) for L-PBF NASA HR-2. The *Md* level of LP-DED NASA HR-1 (0.9134) was used as the critical threshold *Md* value for L-PBF NASA HR-2.

| Alloy | Fe | Ni | Cr | Mo | V | W | Co | Ti | Al | ***Md*** |
|---|---|---|---|---|---|---|---|---|---|---|
| L-PBF NASA HR-2 Formulation I (F1) | 30.85 | 42.00 | 15.00 | 1.80 | 0.10 | 3.20 | 4.00 | 2.80 | 0.25 | **0.9135** |
| L-PBF NASA HR-2 Formulation II (F2) | 30.00 | 41.50 | 15.50 | 3.00 | - | 3.20 | 4.00 | 2.80 | 0.25 | **0.9206** |
| LP-DED NASA HR-1 | 41.20 | 34.00 | 14.60 | 1.80 | 0.30 | 1.60 | 3.80 | 2.40 | 0.25 | **0.9134** |

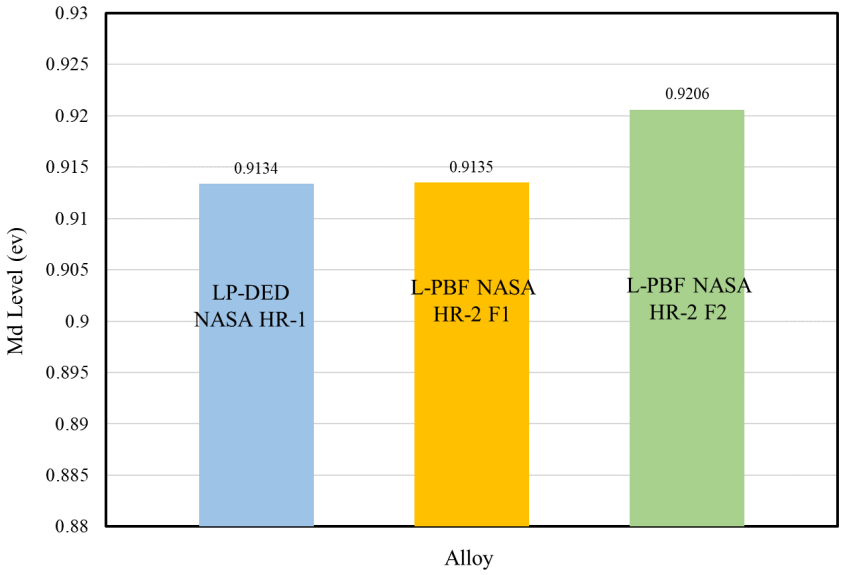


**Figure 1.** *Md* comparison for L-PBF NASA-HR-2 and LP-DED NASA HR-1.

## 3.0 Experimental Procedures and Methods

### 3.1 Material and L-PBF Process

The material used in this study was pre-alloyed NASA HR-2 powder supplied by PAC (Powder Alloy Corporation), located in Loveland, Ohio. The analyzed chemical composition of NASA HR-2 powder and its specification are provided in **Table 2**. The specified powder size distribution is between 10 and 45 μm (+35 mesh/1,250 mesh). The morphology of powders was observed using Hitachi scanning electron microscopy (SEM) with an accelerating voltage of 15 kV. The SEM image showing the typical NASA HR-2 powder morphology for the L-PBF process is presented in **Figure 2**. NASA HR-2 powder has mostly a spherical shape with occasional satellites and agglomerations. These satellites are believed to form when the faster-solidified finer particles adhere to the molten or semi-solid surface of the coarser particles due to the in-flight collisions among the particles during the gas atomization process **[19]**.

**Table 2.** Analyzed chemical composition (wt%) of NASA HR-2 powder and its specification.

| **Wt.%** | **NASA HR-2 Formulation I** | | | | **NASA HR-2 Formulation II** | | | |
|---|---|---|---|---|---|---|---|---|
| **Element** | **Analyzed** | **Nominal** | **Min** | **Max** | **Analyzed** | **Nominal** | **Min** | **Max** |
| Fe | 31.18 | 30.85 | 30.4 | 31.3 | 30.99 | 30 | 29.6 | 30.4 |
| Ni | 41.9 | BAL | | | BAL | 41.5 | | |
| Cr | 15.19 | 15 | 14.7 | 15.3 | 15.65 | 15.5 | 15.2 | 15.8 |
| Co | 3.95 | 4 | 3.8 | 4.2 | 3.8 | 4 | 3.8 | 4.2 |
| Mo | 1.84 | 1.8 | 1.3 | 2 | 2.98 | 3 | 2.8 | 3.2 |
| W | 2.96 | 3.2 | 3 | 3.4 | 3.14 | 3.25 | 3 | 3.4 |
| Ti | 2.59 | 2.8 | 2.7 | 2.9 | 2.55 | 2.8 | 2.7 | 2.9 |
| V | 0.1 | 0.1 | 0.05 | 0.15 | | | | |
| Al | 0.26 | 0.25 | 0.2 | 0.3 | 0.24 | 0.25 | 0.2 | 0.3 |
| S | <0.01 | | | 0.005 | <0.01 | | | 0.005 |
| P | <0.01 | | | 0.005 | <001 | | | 0.005 |
| C | 0.01 | | | 0.03 | 0.01 | | | 0.03 |
| Si | 0.02 | | | 0.05 | 0.02 | | | 0.05 |
| B | <0.05 | | | 0.005 | <0.05 | | | 0.005 |
| Mn | 0.03 | | | 0.05 | 0.03 | | | 0.05 |
| H | 3 ppm | | | <50 ppm | 3 ppm | | | <50 ppm |
| O | 240 ppm | | | <300 ppm | 610 ppm | | | <300 ppm |
| N | 97 ppm | | | <200 ppm | 78 ppm | | | <200 ppm |

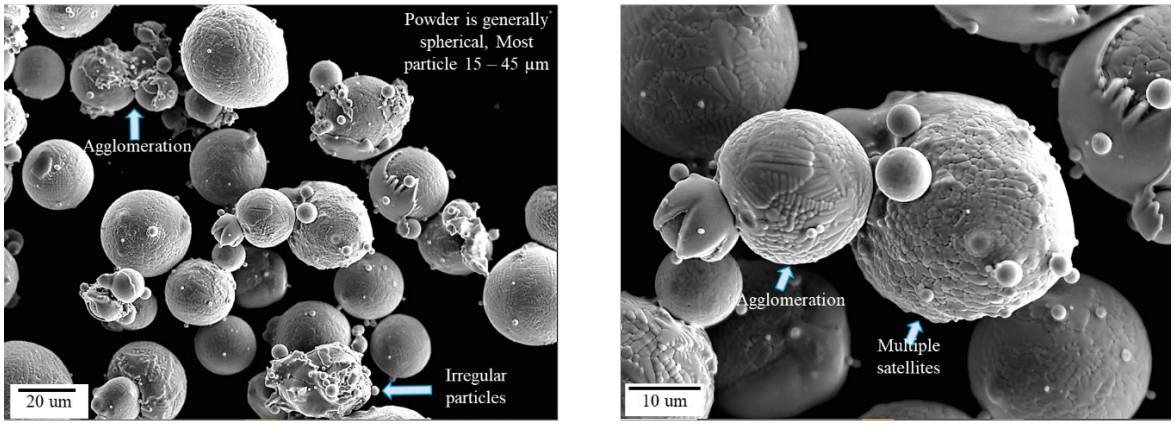


**Figure 2.** SEM images showing NASA HR-2 powder particle morphology (formulation II).

The manufacturing of L-PBF NASA HR-2 samples was performed in an EOS M100 system at MSFC. A screen size of 63 µm was used to filter out large powder particles. The scanning strategy includes re-melting of each layer, where the layer is scanned with a rotation of 67° between the scanning vectors. It has been reported that a 67° rotation in the scanning direction results in different heat flow direction in successive layers. As a result, grain orientation is more random without a particular predominant crystallographic texture in the microstructure. The reduced anisotropy in microstructure can be attributed to the disruptive grain growth caused by the rotating laser scanning path in the sample **[20]**. It must be noted that the M100 system built samples with a restriction angle of 30° to avoid laser scanning parallel to the Ar gas flow direction (y-direction). The 67° rotation angle was skipped and rotated by an additional 67° when the scanning direction was within a range of ± 30° from the y-direction **[21]**, as shown in the red corridors in **Figure 3**. In addition, the laser scanned area is partitioned into 5-mm-wide stripes with 0.1 mm overlap so that the laser tracks are not appreciably large. L-PBF, laser power, scanning speed, hatch spacing, and layer thickness are the typical process parameters. Parameter development was performed to determine the optimum parameter that can produce defect-free and dense parts. An illustration of parameter development sample fabrication via the L-PBF process is shown in **Figure 4**. The sample distribution inside the machine for parameter development, metallography, and tensile testing is shown in **Figure 5**. The round bar tensile samples were deposited to a length of 2.5 inches and 0.375 inches in diameter.

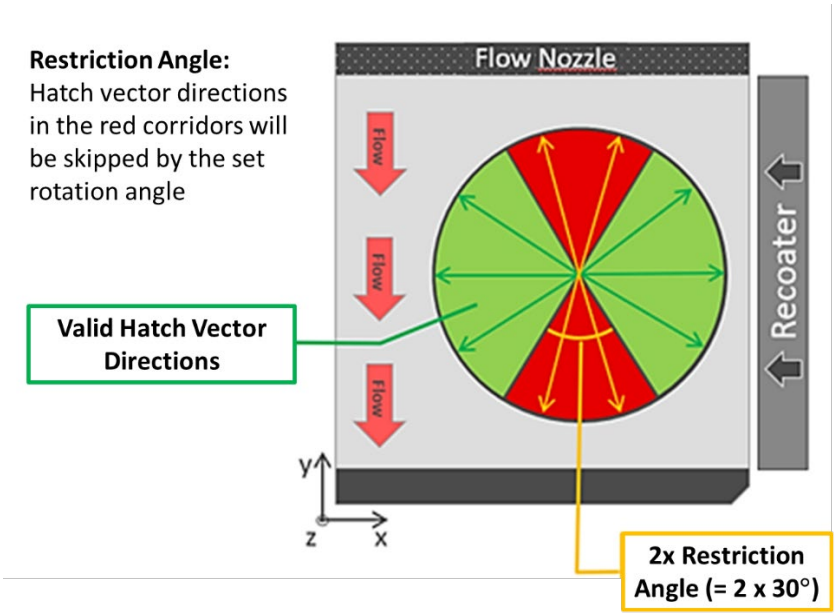


**Figure 3**. The L-PBF parameter for NASA HR-2 has a restriction angle as shown in the red corridors. The 67° rotation angle was skipped and rotated by an additional 67° when the scanning vector was within a range of ± 30° from the y-direction.

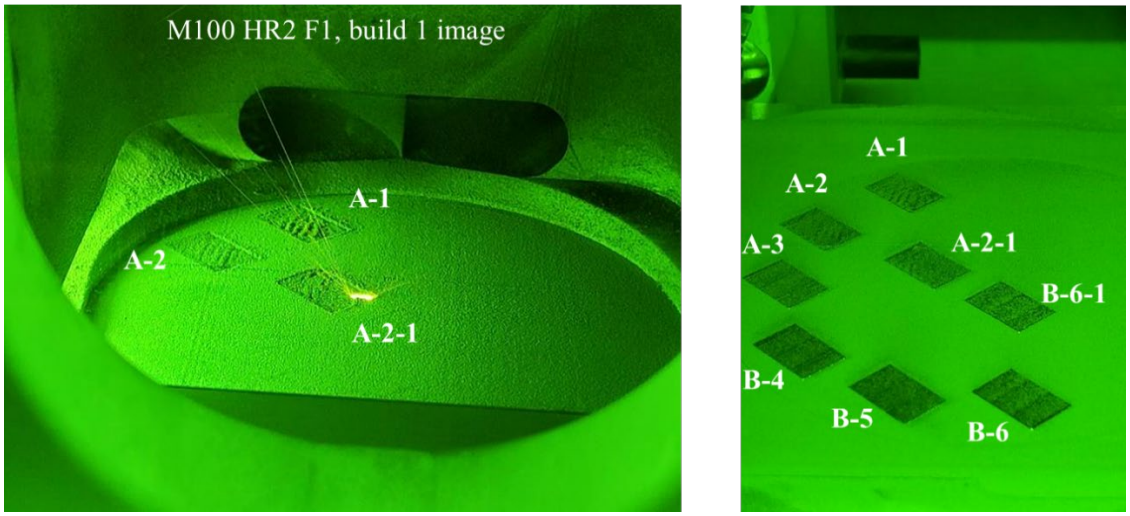


**Figure 4.** An illustration of NASA HR-2 parameter development sample fabrication via L-PBF.

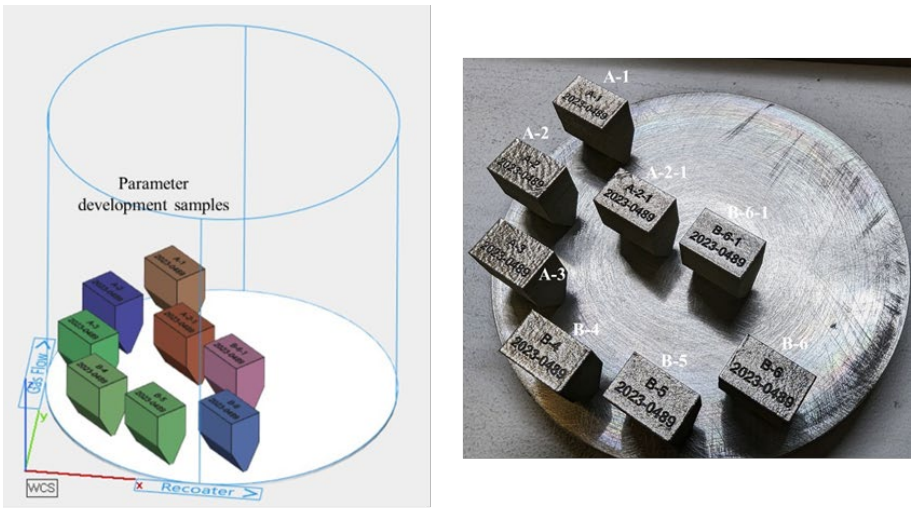


(a)

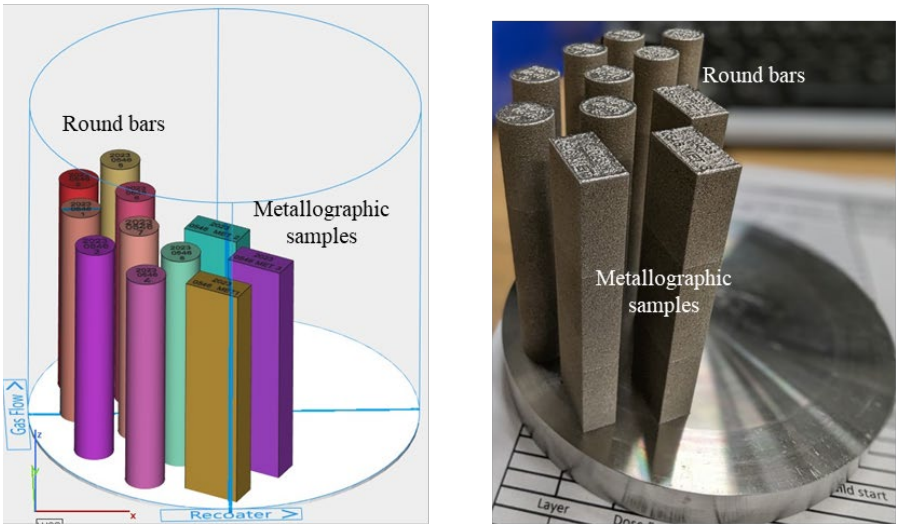


(b)

**Figure 5**. Sample distribution inside the machine for (a) parameter development, (b) metallography and tensile testing. The round bar tensile samples were deposited to a length of 2.5 inches and 0.375 inches in diameter.

### 3.2 Differential Scanning Calirimetry

Differential scanning calirimetry (DSC) was used to analyze the melting solidification behavior of NASA HR-2 powder. DSC was performed using virgin NASA HR-2 powder on a TA SDT Q600 thermal analyzer. The atmosphere was high-purity Ar gas, and an $A_2O_3$ empty crucible was used as the reference sample. Samples were heated from room temperature to 1,480 °C at 20 °C/min, and cooling was also performed using the same rate down to 600 °C. The endothermic peaks indicate melting reaction, while the exothermic peaks signify solidification reaction. The DSC effort aims at obtaining a better understanding of melting and solidification behaviors for NASA HR-2.

### 3.3 Heat Treatment

After L-PBF deposition, the as-built samples require post-processing heat treatment to attain the desirable microstructure and material properties. The heat treatment steps include stress relief, HIP (Hot Isostatic Pressing), solution anneal, and an aging treatment. The as-built samples received stress-relief treatment in vacuum at 1,950 °F/1.5 h with a slow furnace cool. After stress relief, the samples were subjected to a HIP cycle at 2,125 °F/15 ksi/3 h. Then, the samples were solution-annealed at 1,950° F/1 h in vacuum with an Ar quench. Finally, a two-step aging cycle was performed at 1,275 °F/16 h + 1,150 °F/16 h (total 32 hours) in a vacuum furnace to complete the heat treatment process.

### 3.4 Metallography and SEM Analysis

Selected L-PBF NASA HR-2 specimens were metallurgically characterized after heat treatment and mechanical testing. Specimens were sectioned, mounted, ground, and polished using standard metallographic procedures with a series of 220–2,000 grit paper and 3-μm diamond suspension on 0.05-μm alumina pads. Chemical etching was conducted with waterless Kaling's reagent immersed for 5–10 seconds. Fresh acedic glyceregia exchant was used to reveal the melt pool structrue of as-built samples. Microstructures of as-deposited and heat-treated L-PBF NASA HR-2 were examined via optical (Leica DMi8 A) and SEM (Hitachi S-3700N). High-resolution optical montage images were taken to document the microstructure for the entire sample.

### 3.5 Mechanical Testing

Tensile testing was performed in ambient air with a strain rate of 0.5 in/in/min across four temperatures: –423 °F, –320 °F, room temperature, and 1,200 °F. Tests at 1,200 °F were performed using a Mayes elevated temperature extensometer (Model: R3/8 Block 2) on an Instron load frame equipped with a 250-kN load cell, in accordance with ASTM E21 (Standard Test Methods for Elevated Temperature Tension Tests of Metallic Materials). Room temperature testing was conducted using an Instron 5582 load frame equipped with a 100-kN load cell and an Instron model 2620 extensometer, following ASTM E8 (Standard Test Methods for Tension Testing of Metallic Materials). Smooth tensile testing performed at room temperature in ambient air was intended to provide baseline tensile properties without the influence of hydrogen. Tensile testing was also performed in 5-ksi high-pressure $GH_2$ environments at the NASA/MSFC Hydrogen Test Facility (HTF) in test cell 23 (TC-23). The smooth tensile sample had a uniform gauge, 0.188 inch in diameter by 0.75 inch in length. The specified surface finish (Ra, value of arithmetic mean surface roughness) for the gauge section was 32 μin or better. Shape and dimension of the smooth tensile specimen used for testing at ambient temperature in a 5-ksi $GH_2$ environment is shown in **Figure 6**. Final machining of the gauge section was performed by low stress grinding in accordance with ASTM standard G142. Smooth tensile testing in hydrogen was performed at a pre-yield strain rate of 0.005 in/in/min to failure. Fracture elongation was obtained based on the change in the total length of the specimen gauge (0.75-inch gauge length) before and after the test. HEE susceptibility was evaluated by the relative fracture elongation, which is defined as the ratio of fracture elongation in high-pressure $GH_2$ to that in ambient air.

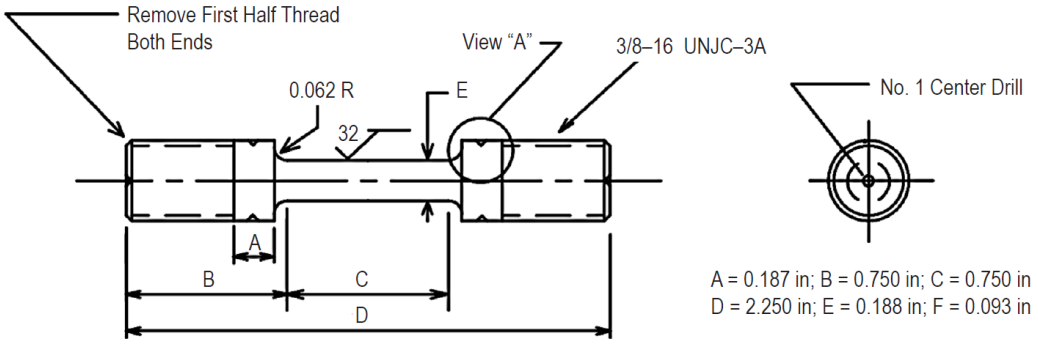


**Figure 6.** Geometry and dimensions of the smooth tensile specimen used for testing in a 5-ksi $GH_2$ environment at ambient temperature. All dimensions are in inches. The specified surface finish (Ra) on the gauge surface is 32 µin or better for specimens to be tested in hydrogen. Low stress grinding (LSG) was used to produce specimens with the specified surface finish.

## 4.0 Results and Discussion

### 4.1 Melting and Solidification Characteristics

DSC was used to analyze the melting and solidification behaviors of NASA HR-2 powder. **Figure 7** shows the heating and cooling DSC curves for formulation I NASA HR-2 powder. On heating, the powder material exhibits a notable change in heat flow that peaks at approximately 2,552 °F (1,400 °C), as shown in **Figure 7(a)**. There is a second endothermic peak at 2,579 °F (1,415 °C) that represents the on-heating liquidus temperature, as shown in **Figure 7(b)**. During the cooling cycle, there is a distinct solidification peak that starts at approximately 2,566 °F (1,408 °C), followed by a larger exothermic peak at 2,521 °F (1,383 °C) that represents the on-cooling solidus temperature. The solidification temperature range (STR) for F1 L-PBF NASA HR-2 is determined to be 33 °C (58 °F), which is the difference between the on-heating liquidus temperature of 1,415 °C (2,579 °F) and the on-cooling solidus temperature of 1,383 °C (2,521 °F).

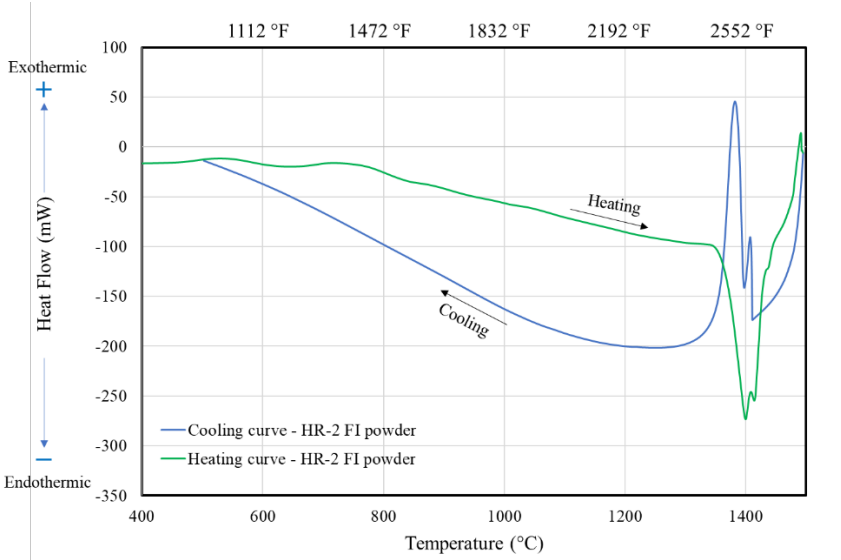

(a)

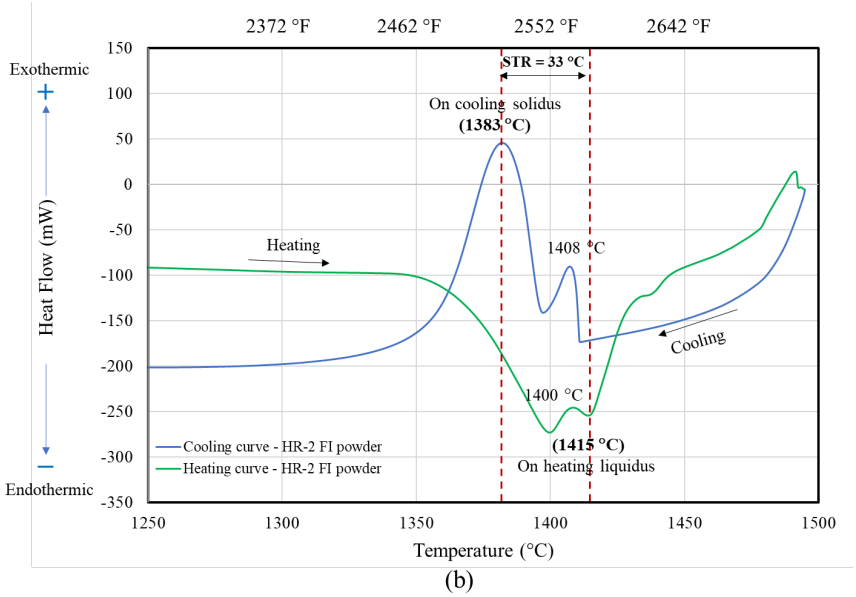


**Figure 7.** (a) DSC heating and cooling curves for formulation 1 NASA HR-2 powder. (b) Close-up view of the melting and solidification peaks in the temperature range of 1,350–1,450 °C (2,462–2,642 °F).

DSC was also performed for formulation II NASA HR-2 powder to compare the melting and solidification behaviors between two different formulations. The DSC curves for formulation II NASA HR-2 powder are shown in **Figure 8**. The melting and solidification characteristics of formulation II powder look very similar to that of formulation I powder. There are also two endothermic peaks on the heating curve and two exothermic peaks on the cooling curve. The on-heating liquidus and on-cooling solidus temperatures are determined to be 2,574 °F (1,412 °C) and 2,518 °F (1,381 °C), respectively. The STR for formulation II L-PBF NASA HR-2 is determined to be 31 °C (56 °F) as shown in **Figure 8(b)**. It has been reported that the susceptibility to weld solidification cracking in Ni-based superalloys is affected by STR and the amount and distribution of the terminal liquid **[22]**. STR controls the size of the semi-solid crack-susceptible region that is surrounded by the liquid weld pool. A narrow STR is preferred as a relatively smaller STR will produce a smaller semi-solid crack-susceptible region, thus decreasing the weld cracking susceptibility. Metal additive manufacturing (such as L-PBF) is fundamentally a repeated welding process where the layer-by-layer growth of the component is achieved through local melting of metal powder by a laser energy source. NASA HR-2 has a very narrow STR that is only 56–58 °F (31–33 °C) wide. Therefore, it is anticipated that NASA HR-2 will have very low solidification cracking susceptibility when building components using the L-PBF process.

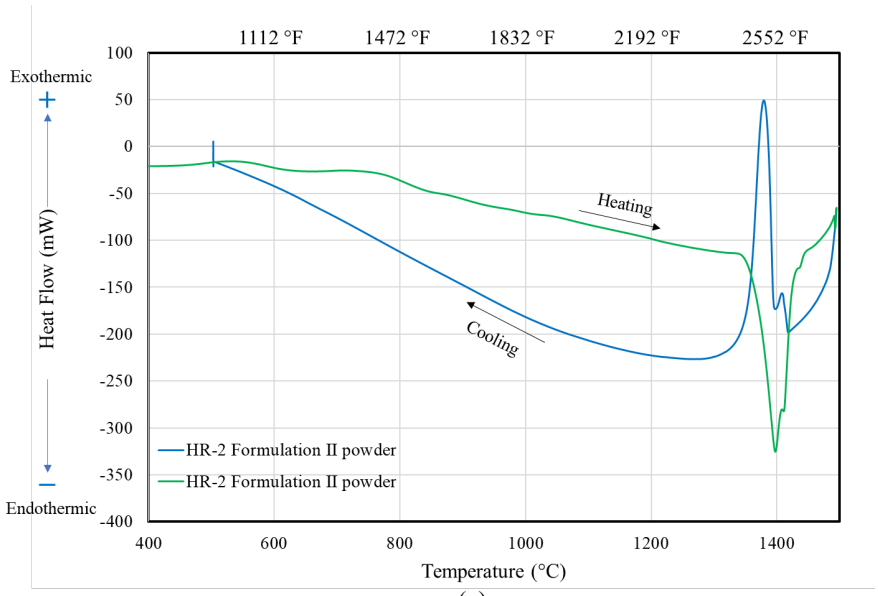


(a)

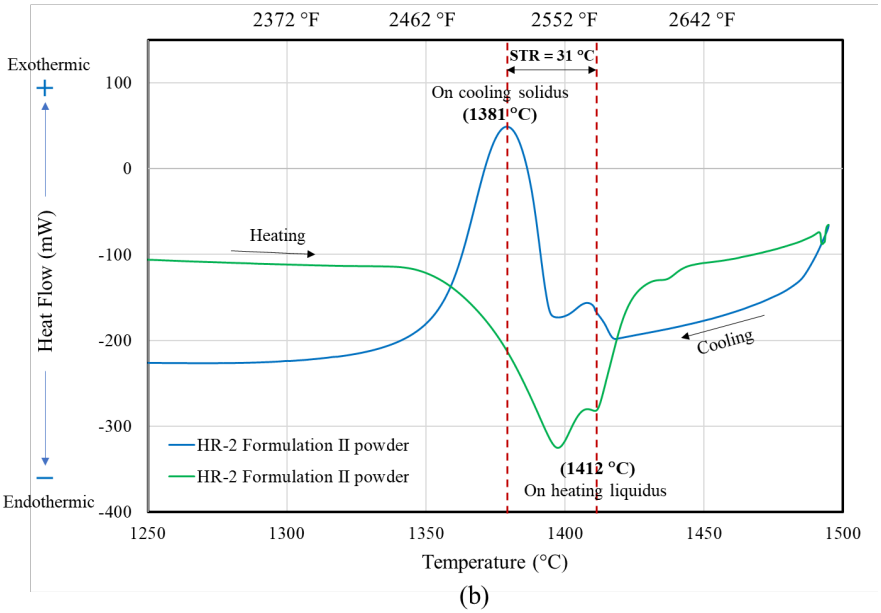


(b)

**Figure 8.** (a) DSC heating and cooling curves for formulation II NASA HR-2 powder. (b) Close-up view of the melting and solidification peaks in the temperature range of 1,350–1,450 °C (2,462–2,642 °F).

### 4.2 L-PBF Parameter Development

During the L-PBF parameter development stage, six different sets of core process parameters were employed to fabricate samples. As shown in **Table 3**, specimens were fabricated by varying laser power, scan speed, and hatch spacing, while keeping the layer thickness constant. The laser power varies from 107 to 170 W, the scan speed and hatch spacing change from 827–1,500 mm/s

and 0.055–0.07 mm, respectively. The layer thickness is kept at 0.02 mm for all parameters. Parameter A-1 has the highest volumetric energy density and A-3 has the lowest volumetric energy density. Relative processing time, which denotes the time (seconds) needed to print a 2,500 $mm^2$ area, is also given in **Table 3**. An illustration of L-PBF NASA HR-2 parameter development samples on the building plate is shown in **Figure 5(a)**. Developing a process parameter that can improve parts quality and maintain an acceptable processing time is a crucial objective for L-PBF parameter development.

**Table 3.** L-PBF parameters for the fabrication of parameter development samples. Relative processing time denotes the time (seconds) needed to print a 2,500 $mm^2$ area.

| Parameter | Power (W) | Scan Speed (mm/s) | Hatch Spacing (mm) | Layer Thickness (mm) | Volumetric Energy Density ($J/mm^3$) | Relative Processing Time (s) |
|---|---|---|---|---|---|---|
| A-1 | 170 | 1,500 | 0.055 | 0.02 | 103.03 | 30.30 |
| A-2 | 170 | 1,500 | 0.060 | 0.02 | 94.44 | 27.78 |
| A-3 | 170 | 1,500 | 0.065 | 0.02 | 87.18 | 25.64 |
| B-4 | 170 | 1,300 | 0.070 | 0.02 | 93.41 | 27.47 |
| B-5 | 140 | 1,200 | 0.060 | 0.02 | 97.22 | 34.72 |
| B-6 | 107 | 827 | 0.070 | 0.02 | 92.42 | 43.19 |

### 4.3 Top Surface Quality

Surface roughness is one of the most important quality parameters in the L-PBF process, as the surface of an additively manufactured part is rougher than that produced through traditional manufacturing processes. Various process parameters such as laser power, hatch spacing, layer thickness, and scan speed influence the surface roughness of the final part **[23, 24]**. Poor surface quality can have a negative impact on mechanical properties such as fatigue life **[25, 26]**. Therefore, the top surface roughness and morphology of the parameter-development samples (built with six different parameters) were analyzed and compared to determine the effect of process parameters on the surface quality. **Figure 9** presents SEM images and surface morphology profiles of as-built samples (measured by a scanning laser microscope) that were built with three different parameters (A-1, B-4, and B-6). As shown, the top surfaces in all cases have some un-melted and/or partially melted powder particles but are free of defects such as lack of fusion and hot cracking. The distance between a peak and a valley can be seen clearly in the surface morphology/profile images.

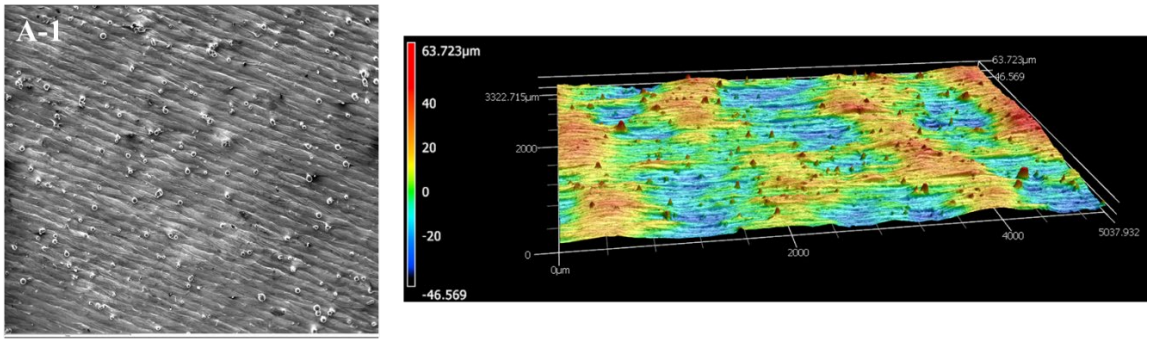


(a)

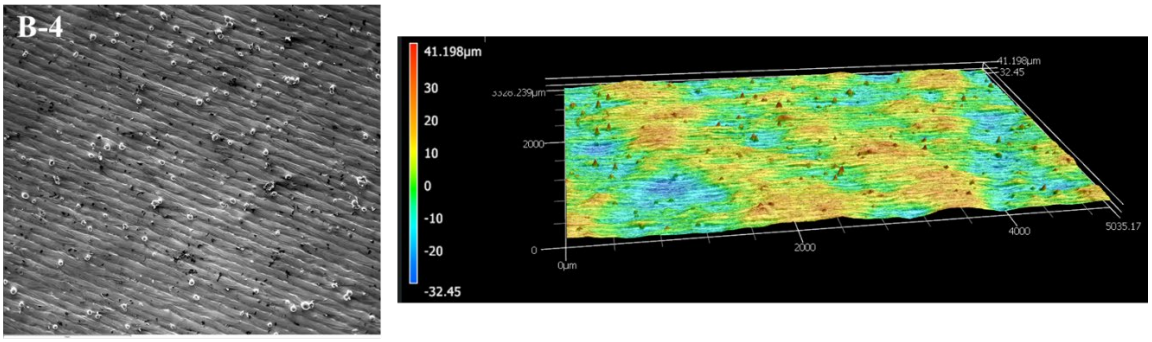


(b)

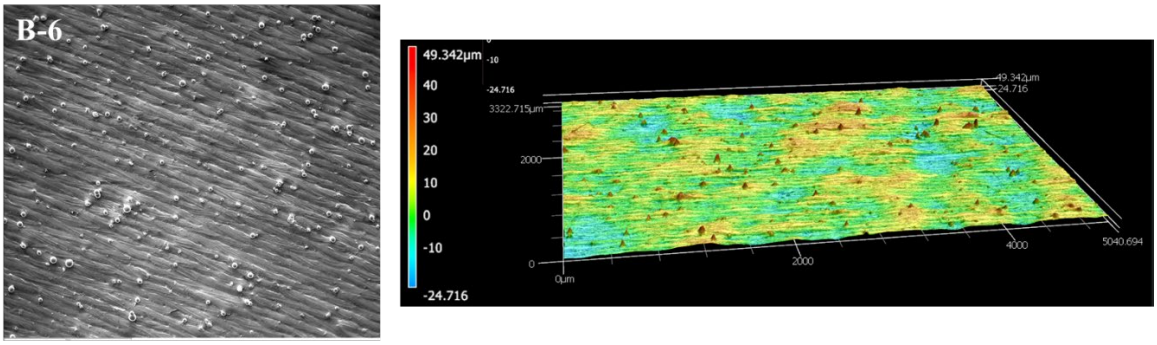


(c)

**Figure 9.** SEM images and surface morphology/profile (measured by a scanning laser microscope) showing top surface quality of as-built samples fabricated with parameters (a) A-1, (b) B-4, and (c) B-6.

**Figure 10** presents the variation of surface roughness (Ra) and waviness (Wa) as a function of L-PBF parameter. It can be seen clearly that A-1 has the highest Ra and Wa, which is likely caused by reduced hatch spacing that increases volumetric energy density. The frequency of remelting and solidification increases when the hatch spacing is reduced. Overheating of the laser track and increased thermal distortion of the processed layer can occur when the hatch distance is reduced too much, leading to a more pronounced Wa and Ra on the part's surface **[23]**. In addition to the

hatch spacing, scanning speed also contributes to the final surface quality of as-built parts as it alters the volumetric energy density and the speed of the L-PBF process **[24]**. As shown in **Figure 10**, the best surface quality is obtained from parameter B-6, which can be attributed to reduced scan speed and laser power. All in all, it can be concluded that developing an optimum process parameter for L-PBF NASA HR-2 is crucial to achieving the desirable surface quality for as-built parts.

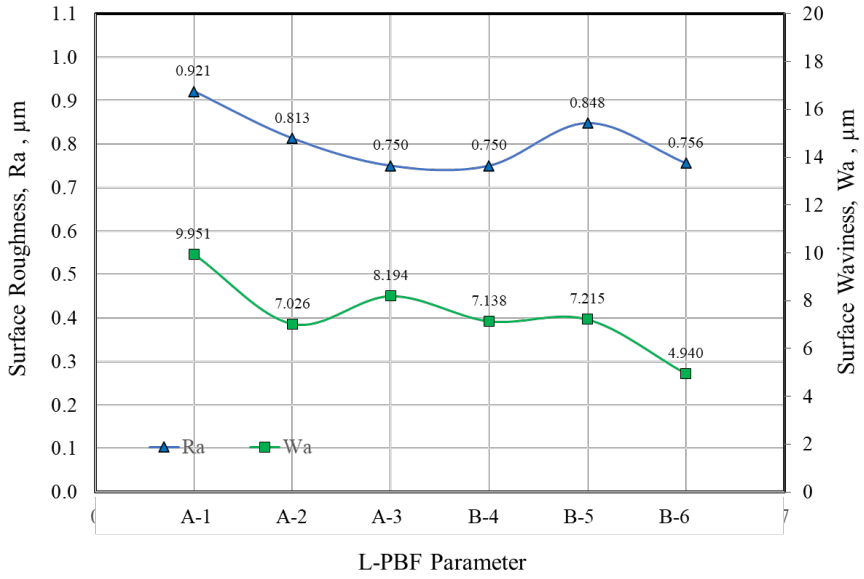


**Figure 10.** Ra and Wa variation as a function of build parameter.

### 4.4 Porosity Analysis

Porosity is a common defect in metal AM parts and can negatively affect mechanical properties. A good build quality should have very low fraction of porosity in the microstructure. Therefore, the influence of process parameters on the void content was explored and compared. Porosity was measured on the parameter development samples that were built with six different L-PBF parameters. Each polished sample was observed via optical microscopy (Leica DMi8 A) to analyze the void content. The micrographs were processed using ImageJ processing software to convert pores into black pixels using a thresholding tool. The percentage of black pixels versus the total number of pixels for each micrograph was determined. Porosity was then calculated by averaging the percentage of black pixels in the micrographs for each parameter per ASTM E2109-01 standard (2014).

Representative optical micrographs of the L-PBF NASA HR-2 (formulation II) samples in the as-polished condition are shown in **Figure 11**. Porosity is very low and varies slightly with the build parameters from 0.01% in sample B-4 to 0.043% in sample B-6. There are no signs of defects, such as lack of fusion and micro-cracks, in the samples. **Figure 12** compares the measured porosity as a function of L-PBF process parameter for both formulations. It is

significant to note that L-PBF NASA HR-2 can achieve very low porosity in the as-built condition. As shown in **Figure 12**, formulation II can achieve lower porosity than formulation I, but the trend of L-PBF parameter effect on porosity is similar for both formulations. Judging from the porosity level, Ra/Wa, and relative processing time, B-4 appeared to be the most promising parameter and was selected to fabricate tensile and metallographic samples.

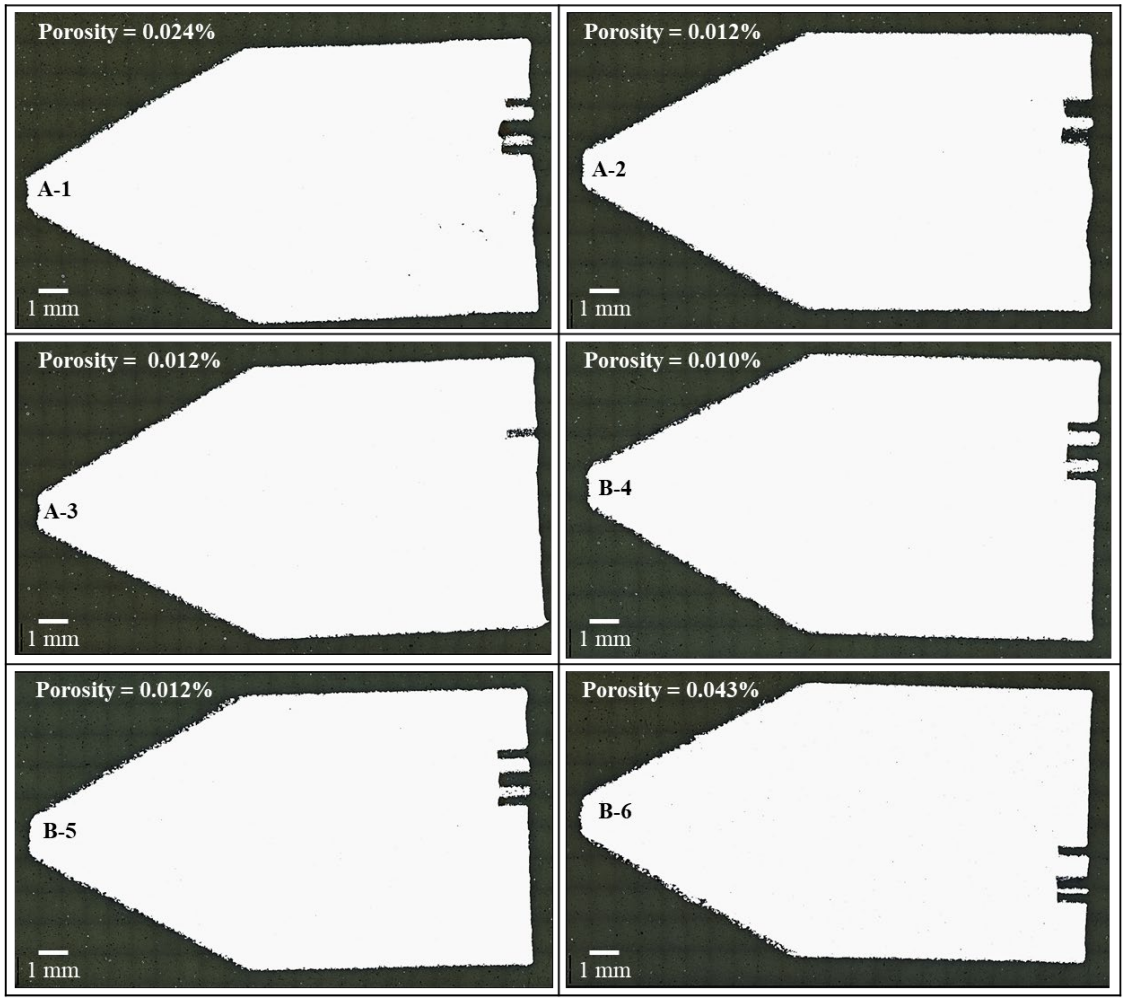


**Figure 11**. Optical micrographs showing L-PBF NASA HR-2 samples (formulation II) in the as-polished condition. Porosity is very low and varies slightly with the build parameters.

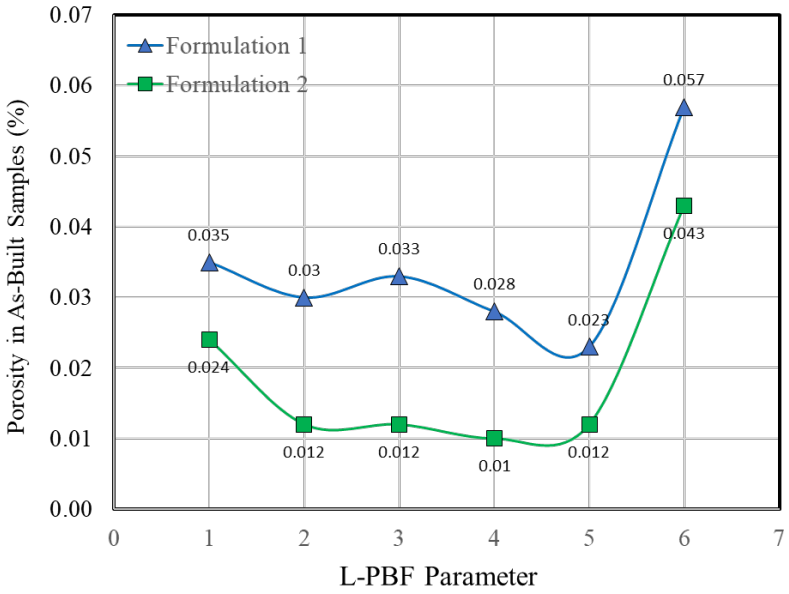


**Figure 12.** Measured porosity vs. process parameter for L-PBF NASA HR-2.

## 4.5 As-Deposited Microstructure

### 4.5.1 As-Deposited Microstructure

The melt pool microstructure characteristics in terms of the size and shape of the melt pools and the distribution of micro-pores were investigated to determine how L-PBF parameters influence the as-deposited microstructure. In the as-built state, the L-PBF-manufactured NASA HR-2 microstructure exhibits an arc-shaped structure due to the layer-by-layer building process. The as-built microstructure in the XZ cross-sections (parallel to the build direction) shows overlapping melt pools as shown in **Figure 13**. The rotation of the scan vectors in every layer by 67° results in complex melt pool traces. It can be seen clearly from the top layers that there are appreciable variations in the melt pool shape and depth due to the change in the build parameters. Melt pool depth for all samples varies from 83–107 µm. Sample A-1 exhibits a higher degree of melt pool overlap than the others as it has the smallest hatch spacing (0.055 mm). As can be seen in **Figure 13**, the depth of melt pool is greater in sample B-6 than in the others, which likely results from the reduction in scan speed from 1,500 mm/s to 827 mm/s. Most pores are spherical, and they are very fine (< 2µm in diameter) and randomly distributed throughout the samples. Studies indicate the formation of fine round pores can be attributed to interlayer melting or Ar gas being trapped within the material **[27,28]**.

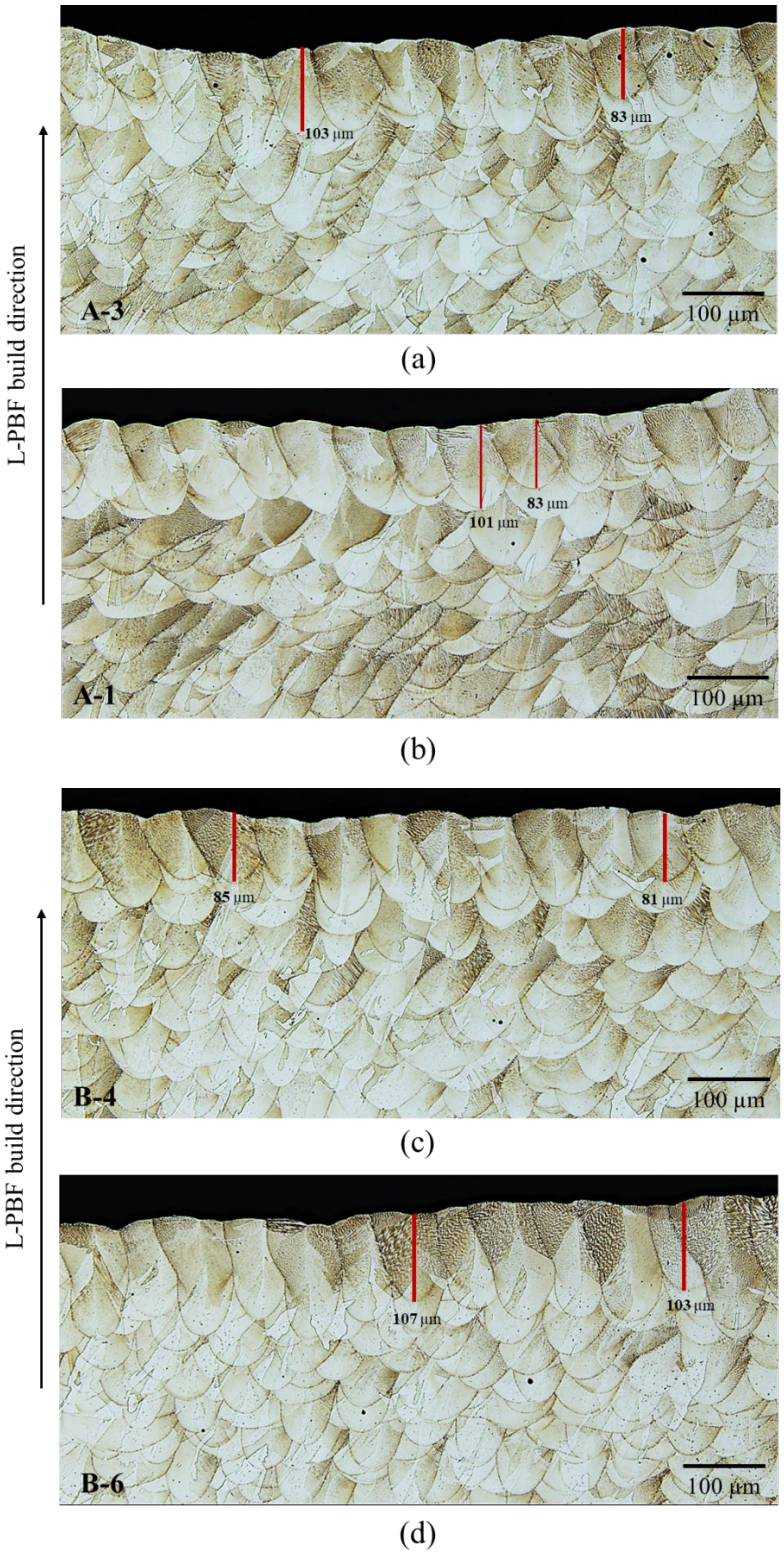


**Figure 13.** The as-built microstructure in the XZ cross-section (parallel to the build direction) showing overlapping melt pools and the top layer for samples (a) A-3, (b) A-1, (c) B-4, and (d) B-6.

**Figure 14** shows the as-built microstructure in the XY cross-section. The cross hatches that rotate between two successive layers can be discerned as there is a diagonal pattern across the micrograph. As shown, the layer is scanned with an angular rotation of 67° between the scanning vectors. It was believed that when a 67° rotation was used, the scan vector direction would not repeat for the maximum number of layers **[29]**. With this scanning strategy, it was reported that a significant reduction in warping, defects, and anisotropy can be achieved in addition to improvised surface roughness **[30]**. This type of hatch pattern is widely adopted by the AM industry **[31]**. A quasi-3D microscopy image showing the as-built microstructure (built with B-4 parameter) in three different orientations (XY, XZ, and YZ planes) is presented in **Figure 15**. Elongated columnar grains can be seen extending through several melt pools on the XZ and YZ planes.

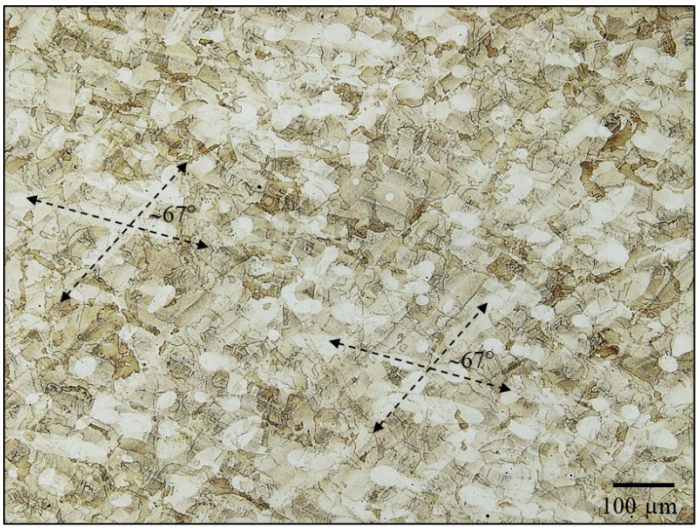


**Figure 14.** The as-built microstructure in the XY cross-section clearly reveals the scanning strategy with an angular rotation of approximately 67° between layers (built with B-4 parameter).

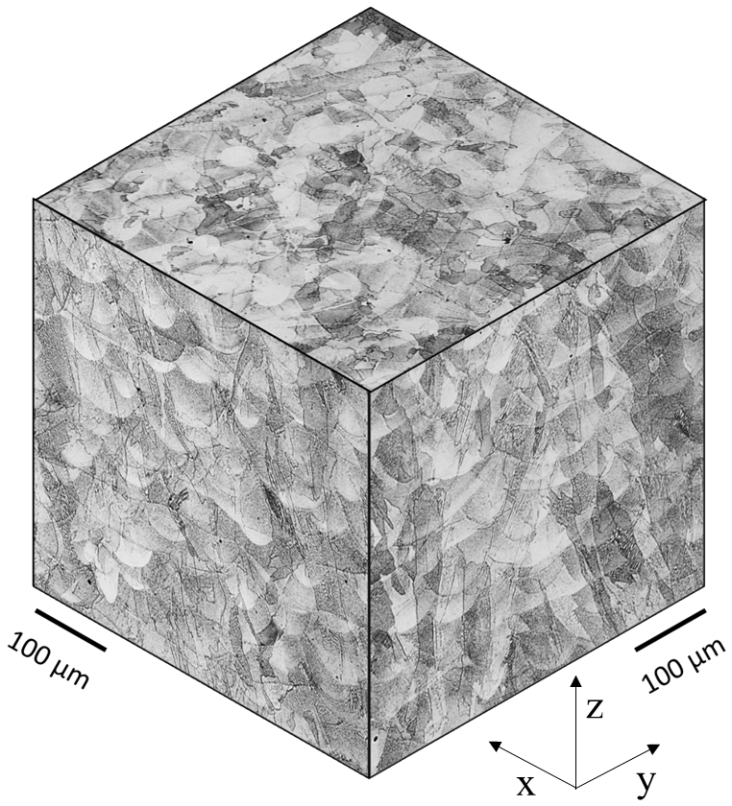


**Figure 15.** Quasi-3D microscopy showing the as-built microstructure (B-4 parameters) in three different orientations, XY, XZ, and YZ. Elongated columnar grains can be seen extending through several melt pools on the XZ and YZ planes.

### 4.5.2 As-Deposited Dendritic Structure and Grain Morphology

In metal AM, unique grain morphologies are created due to the layer-by-layer material deposition, rapid solidification, and heat transfer toward the cooler surrounding material (direction of thermal gradient). To obtain a better understanding of microstructural evolution of NASA HR-2 during the L-PBF process, SEM was used to observe the formation of various dendrite structures in the as-built state. The SEM images showing the as-deposited microstructure of L-PBF NASA HR-2 built with parameters A-1 and B-4 are shown in **Figure 16**. The white dotted line denotes the boundaries between individual melt pools in the build direction (the XZ plane). The growth of dendrites does not exhibit any preferential direction as shown by the yellow arrows. A-1 appears to have a coarser dendritic structure than B-4, which can be attributed to the applied L-PBF parameters. As shown in **Table 3**, parameter A-1 has significantly higher volumetric energy density than B-4. During solidification, local changes in the cooling rate and thermal gradient will alter the dendritic structure. A coarser dendritic structure forms at lower cooling rates (higher volumetric energy density), while a more refined dendritic structure is observed at higher cooling rates (lower volumetric energy density).

The SEM images (see **Fig. 16**) clearly show the characteristic pattern of columnar dendritic structure and epitaxial dendritic growth that is not revealed in the optical images shown in **Figures 13, 14,** and **15**. Grains are mostly columnar and extend across several re-melted layers. The observed epitaxial dendrite growth is a dominant feature in the as-deposited microstructure. The formation of such a feature can be attributed to the direction of thermal gradient and rapid solidification, which promoted the development of a columnar grain structure. The dendritic structure of L-PBF NASA HR-2 exhibits noticeable heterogeneity that can be attributed to different solidification or cooling rates at various locations during the L-PBF process **[32]**. A columnar dendritic structure often grew through several layers, and dendrite spacing is very small (smaller than 1 μm in most areas). Due to the fine dendritic structure, analysis of Ti segregation is not possible via EDS as the interaction volume of the electron beam far exceeded the spacing of dendritic arms **[33]**.

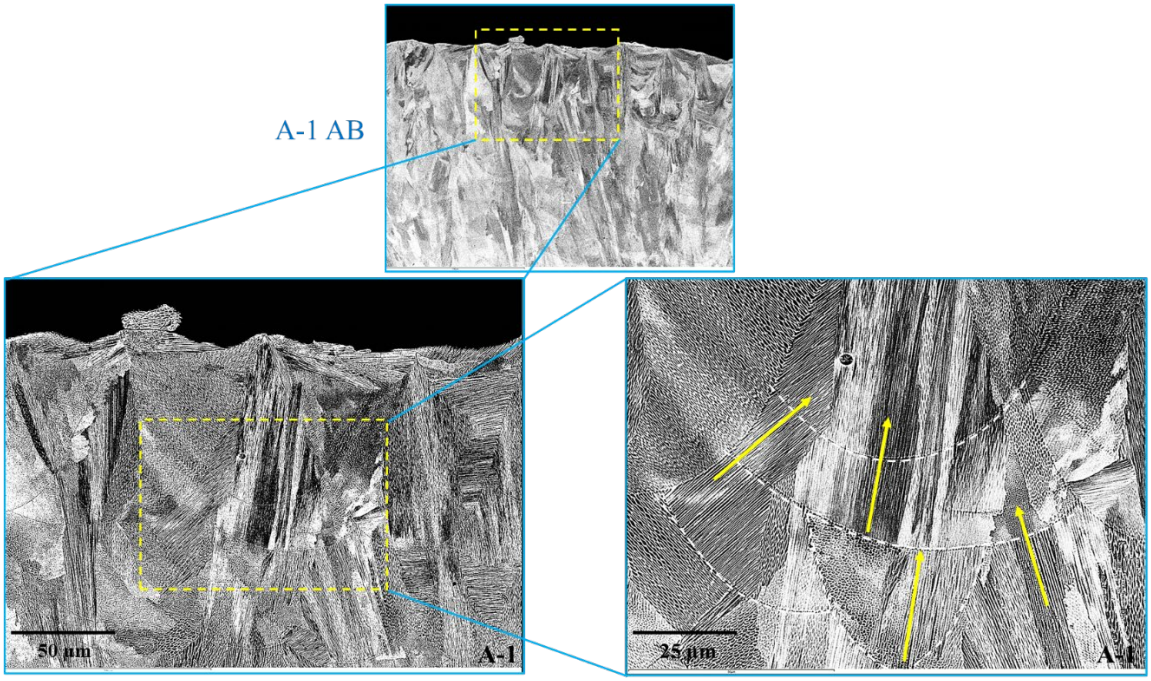


(a)

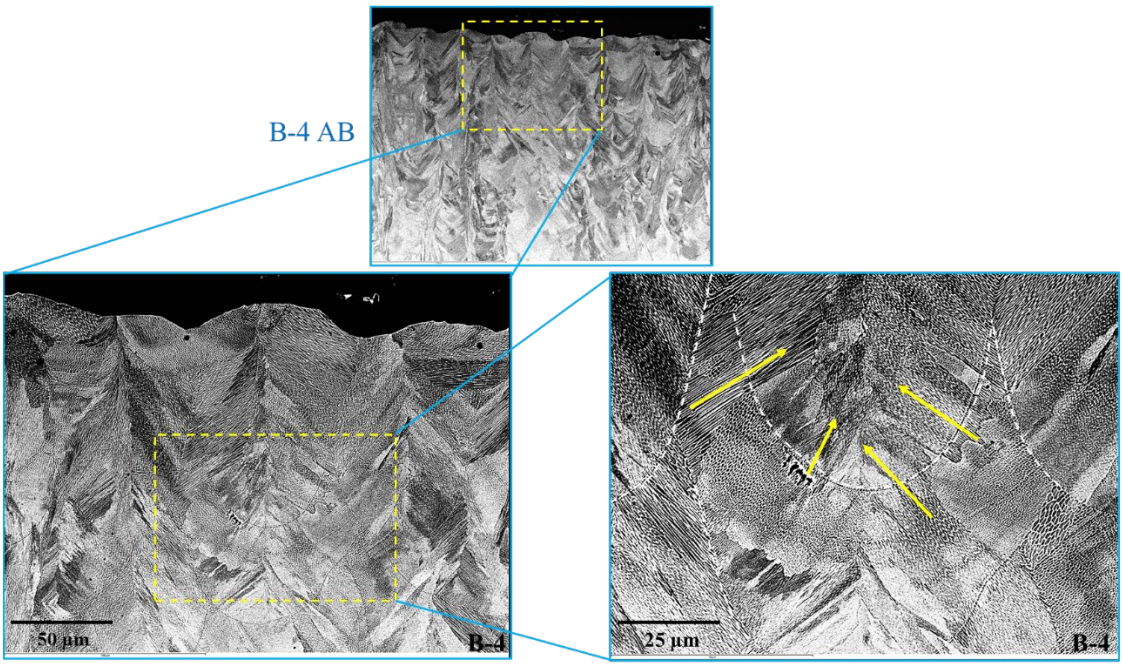


**Figure 16.** SEM images revealing microstructural features of as-built L-PBF NASA HR-2 (on XZ plane) fabricated with (a) parameter A-1 and (b) B-4. The white dotted line denotes the boundaries between individual melt pools and the yellow arrows represent the dendrite growth direction. Melt pool boundaries and dendritic growth often extends through several layers.

## 4.6 Microstructure Evolution After Heat Treatment

### 4.6.1 Post-Processing Heat Treatment

During the L-PBF process, the material is deposited layer by layer by a high-power laser beam and is subjected to complex thermal cycles that include rapid heating above the melting temperature and rapid cooling and solidification of the molten material. Thus, the L-PBF material always has high residual stress, heterogeneous microstructures, porosity, non-uniform chemical composition, and phase distribution. Thermal post-processing (heat treatment) must be used to relieve residual stress, minimize the void content, and achieve the desired microstructure evolution and mechanical properties. The heat treatment for L-PBF NASA HR-2 consists of stress relief, HIP treatment, solution anneal, and aging treatment. A stress relief cycle was performed as the first step prior to removing the parts from the build plate. After stress relief, the samples were subjected to a HIP cycle in an Ar atmosphere to reduce porosity in as-fabricated parts. Then, the samples were solution-annealed in vacuum with an Ar quench to minimize η-phase precipitation. Solution annealing is often referred to as solution treatment or solutioning, which is a specific annealing process that dissolves existing precipitates back into the solution. Finally, the samples were heat treated with a two-step aging cycle in a vacuum furnace to precipitate and grow the strengthening γ′ precipitate. The heat treatment process for L-PBF NASA HR-2 is shown below:

- Stress relief at 1,950 °F for 1.5 hours in vacuum, followed by slow furnace cool,

- HIP at 2,125 °F under a pressure of 15 ksi for 3 hours in an Ar atmosphere,
- Solution annealing at 1,950 °F for 1 hour in vacuum, followed by an Ar quench,
- Two-step aging at 1,275 °F for 16 hours and 1,150 °F for 16 hours in vacuum.

### 4.6.2 Microstructure Evolution after Stress Relief and HIP

**Figure 17** presents the SEM images showing microstructure evolution after heat treatment for formulation II samples built with B-4 parameter. Stress relief treatment involves a recovery process by atomic diffusion from regions of higher stress to regions of lower stress, resulting in the relief of internal strain energy **[34]**. An effective stress relief can mitigate residual stresses and minimize the potential distortions. For L-PBF NASA HR-2, recovery and partial recrystallization occurred during stress relief at 1,950 °F/1.5 h as shown in **Figure 17(b)**. After stress relief, the samples were subjected to a HIP treatment at 2,125 °F to close internal pores, reduce elemental segregation, and promote recrystallization. As shown in **Figure 17(c)**, a complete transformation in microstructure occurs after HIP at 2,125 °F/15 ksi for 3 hours. The as-built microstructure evolves well into fine equiaxed grain structure after HIP treatment. A high degree of recrystallization is desirable for L-PBF NASA HR-2. After HIP, solution anneal and aging processes are performed sequentially to precipitate and grow the strengthening γ′ precipitate ($Ni_3$(Ti, Al)). The primary objective of solution treatment is to dissolve the remnant η phase that may have formed during the slow cooling process after HIP. After completion of the solution anneal cycle in vacuum, the material is rapidly cooled by Ar quench to maintain η-phase-free solid solution. Solution annealing and aging cycles after HIP do not lead to further recrystallization and reduction in grain size as shown in **Figure 17(d)**.

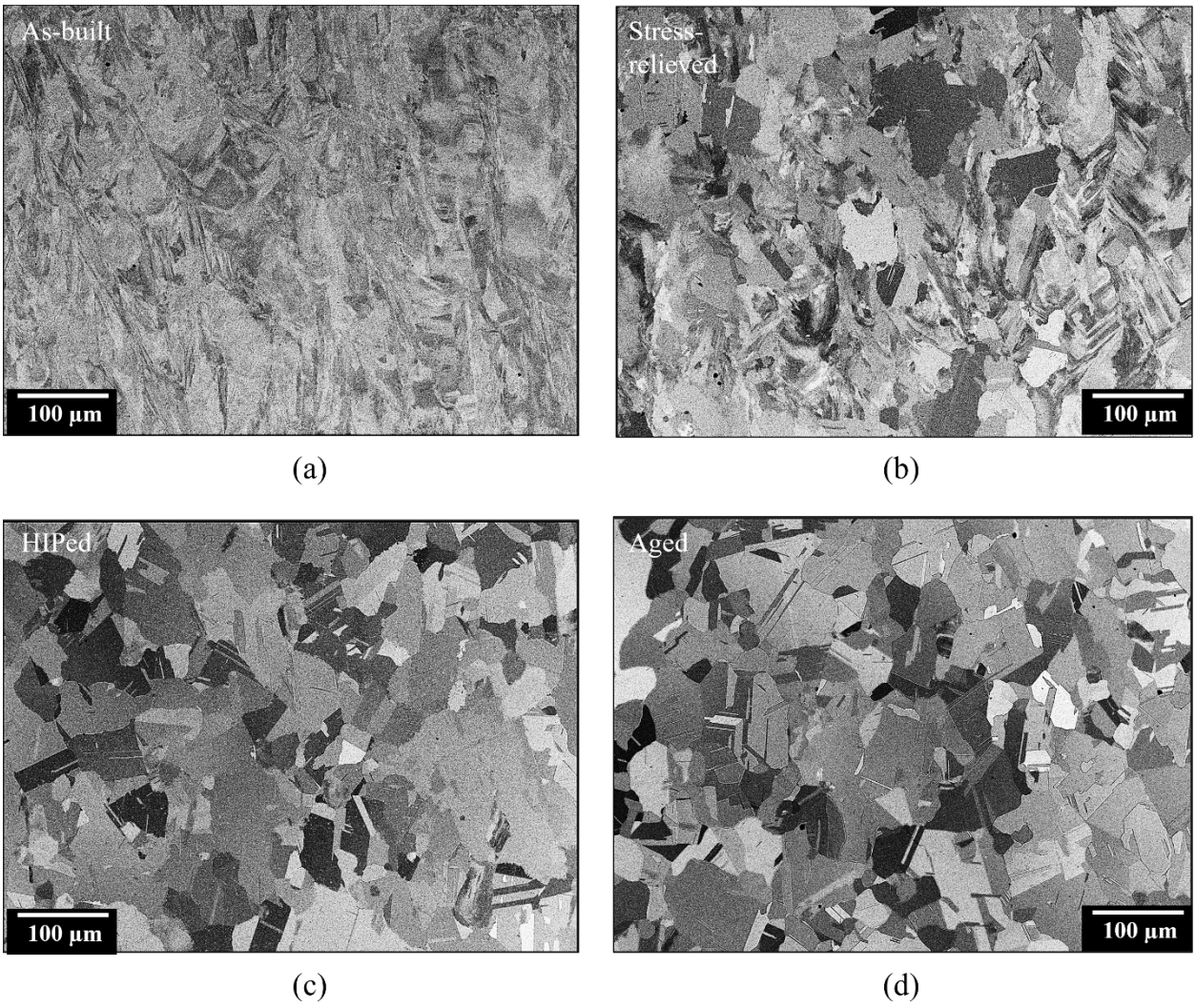


**Figure 17.** SEM images showing microstructure evolution on the XZ plane in (a) as-built condition, and after (b) stress relief, (c) HIP, and (d) solution anneal and age. The sample was built with B-4 parameter. Solution annealing after HIP does not lead to further recrystallization and reduction in grain size.

**Figure 18** shows the influence of L-PBF process parameter on microstructure evolution (on the XZ plane) after HIP. It is obvious that a high degree of recrystallization had taken place after HIP at 2,125 °F/15 ksi/3 h. The driving force for recrystallization is the residual stress from the AM process **[35–38]**. During the L-PBF process, the rapid heating and cooling cycles along with the volume change of the molten metal upon solidification result in buildup of residual stress in the parts. It is apparent that the residual stress in the as-built condition is quite high, which led to a high degree of recrystallization after heat treatment. Overall, the grain size of L-PBF NASA HR-2 after HIP is quite small, and many grains in the material are smaller than 50 µm in diameter. As can be seen in **Figure 18**, B-4 exhibits a higher degree of recrystallization and smaller gain size than the others.

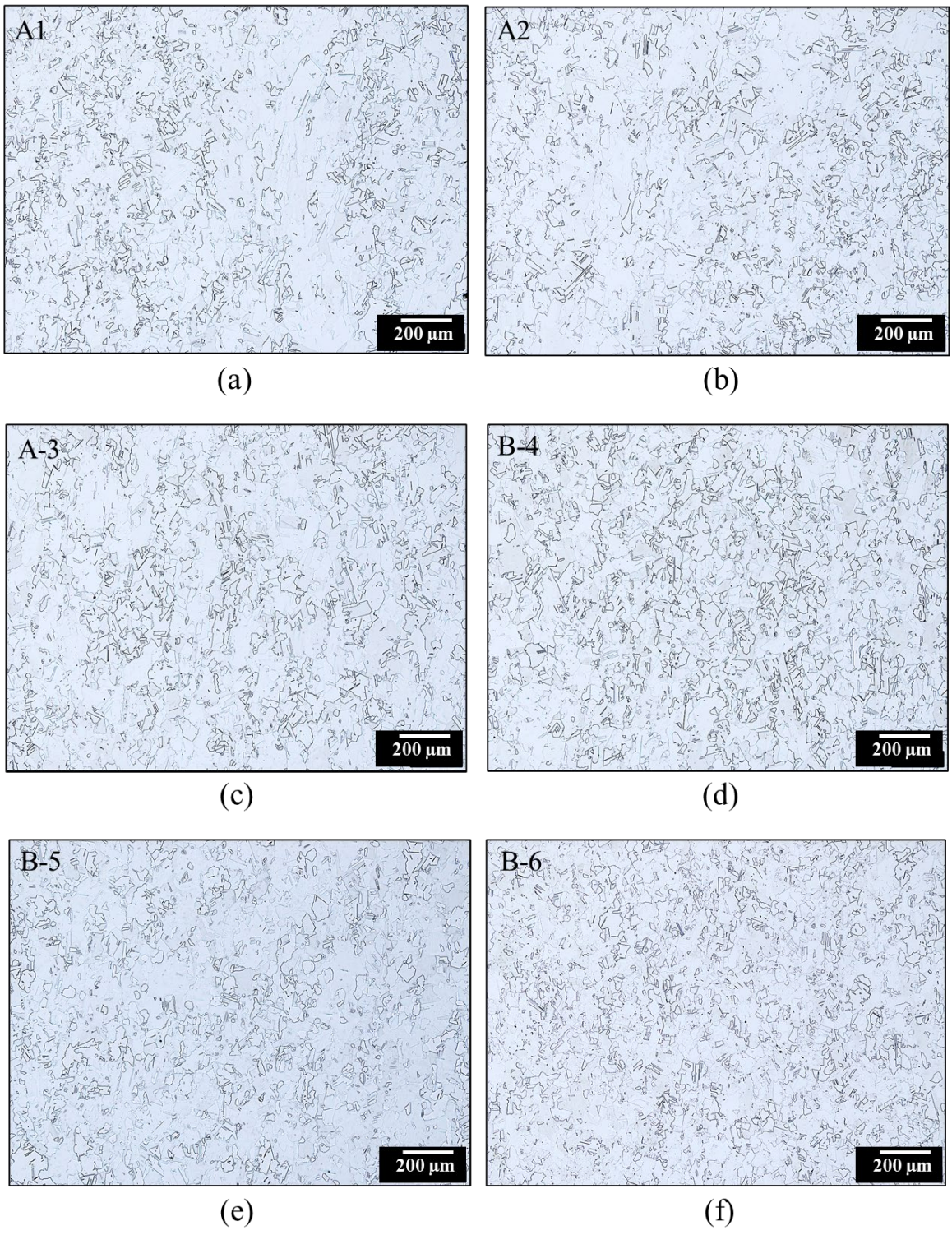


**Figure 18.** Varying degrees of recrystallization occurred after the material was HIPed at 2,125 °F/15 ksi/3 h. The samples were built with (a) A-1, (b) A-2, (c) A-3, (d) B-4, (e) B-5, and (f) B-6 parameters. The viewing surface is the XZ plane. Sample B-4 exhibits a higher degree of recrystallization and smaller gain size than the others.

In general, a high degree of recrystallization is desirable as it can reduce anisotropy in mechanical properties. It has been reported that the tensile properties of L-PBF IN738LC strongly depend on whether recrystallization was completed **[39]**. A low degree of recrystallization will result in undesirable anisotropy that may significantly affect mechanical properties. Mechanical anisotropy was observed in additively manufactured Hastelloy X with a low degree of recrystallization **[40]**. The un-recrystallized columnar grains reduce the total number of grain boundaries along the build direction (BD), leading to higher fracture elongation and lower ultimate tensile strength (UTS) when loaded along the BD. In contrast, the grain size in the transverse direction (TD) was approximately three times smaller than that in the BD and therefore results in a higher UTS and lower fracture elongation **[40]**. Anisotropy in tensile behavior can be attributed to a low degree of recrystallization that changes grain orientation, grain shape, and crystallographic texture **[41]**. The selection on an optimum L-PBF parameter to fabricate tensile samples is evaluated based on various quality factors such as surface roughness, porosity, microstructure evolution after heat treatment, and relative processing time. After a thorough evaluation on the quality factors, B-4 appears to be the most promising parameter and was selected to fabricate tensile samples. The grain structure of B-4 after heat treatment in the XY and YZ orientations is shown in **Figure 19**.

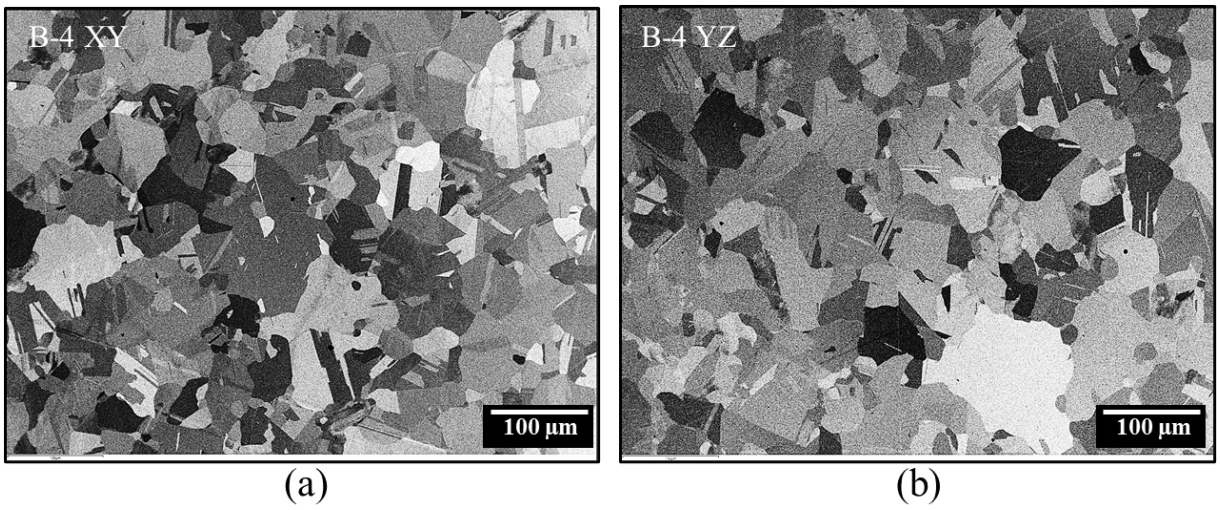


**Figure 19.** SEM images showing recrystallized grain structure after heat treatment in (a) XY and (b) YZ orientations for sample built with B-4 parameter.

Alloy chemistry also affects recrystallization behavior after post-processing heat treatment. 3D images showing microstructure evolution before and after post-processing heat treatment for samples built with B-4 parameter are shown in **Figure 20** (for formulation I) and **Figure 21** (for formulation II). Formulation II samples appear to have a higher degree of recrystallization than formulation I samples after stress relief. However, the grain structure looks similar for both formulations in fully heat-treated condition. After a thorough evaluation on the effects of alloy chemistry on parts quality, formulation II appears to be more promising than formulation I as formulation II samples have lower porosity (see **Fig. 12**) and a slightly higher degree of recrystallization than formulation I samples.

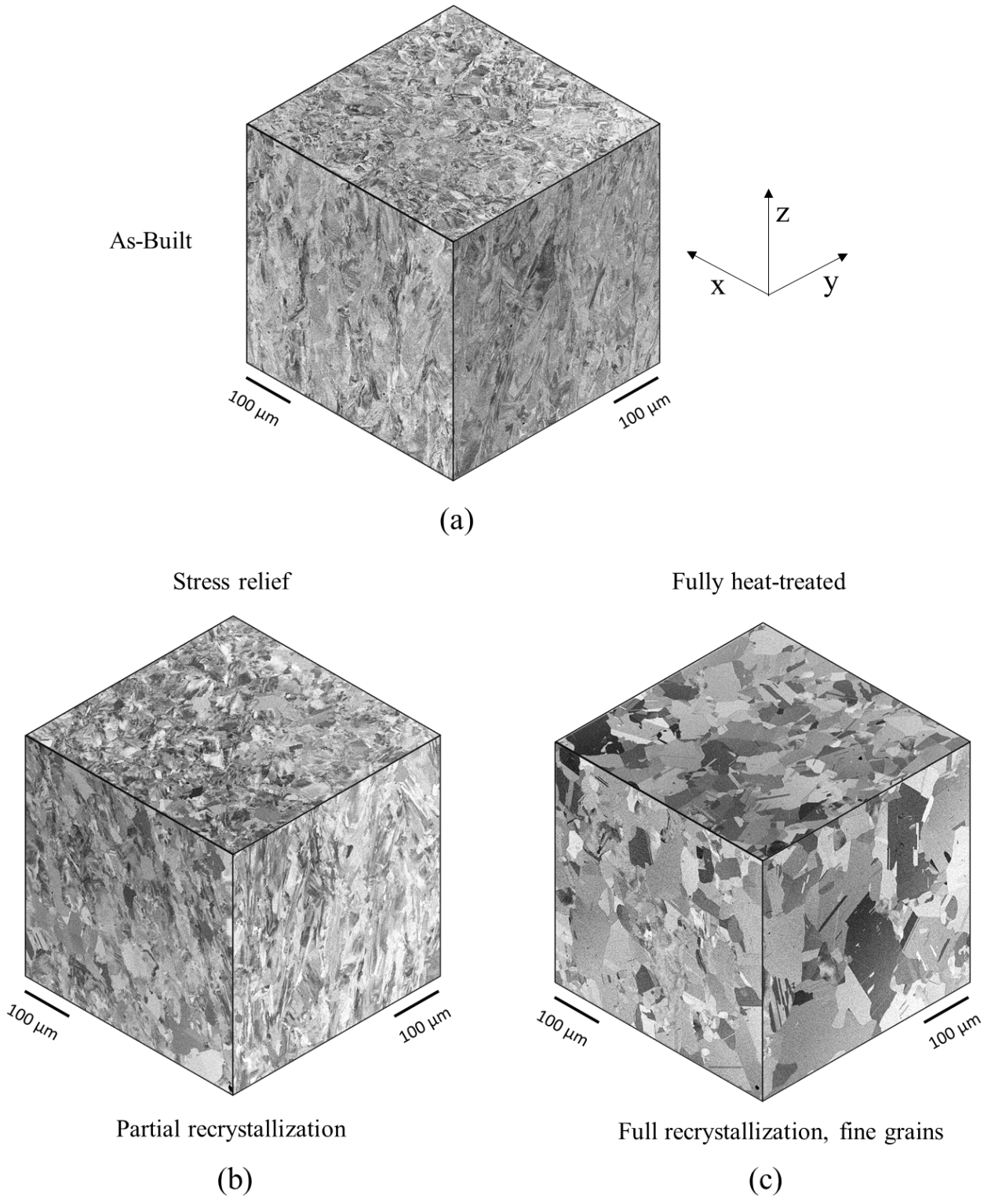


**Figure 20.** Quasi-3D images showing microstructure evolution of B-4 samples before and after post-processing heat treatment (formulation I).

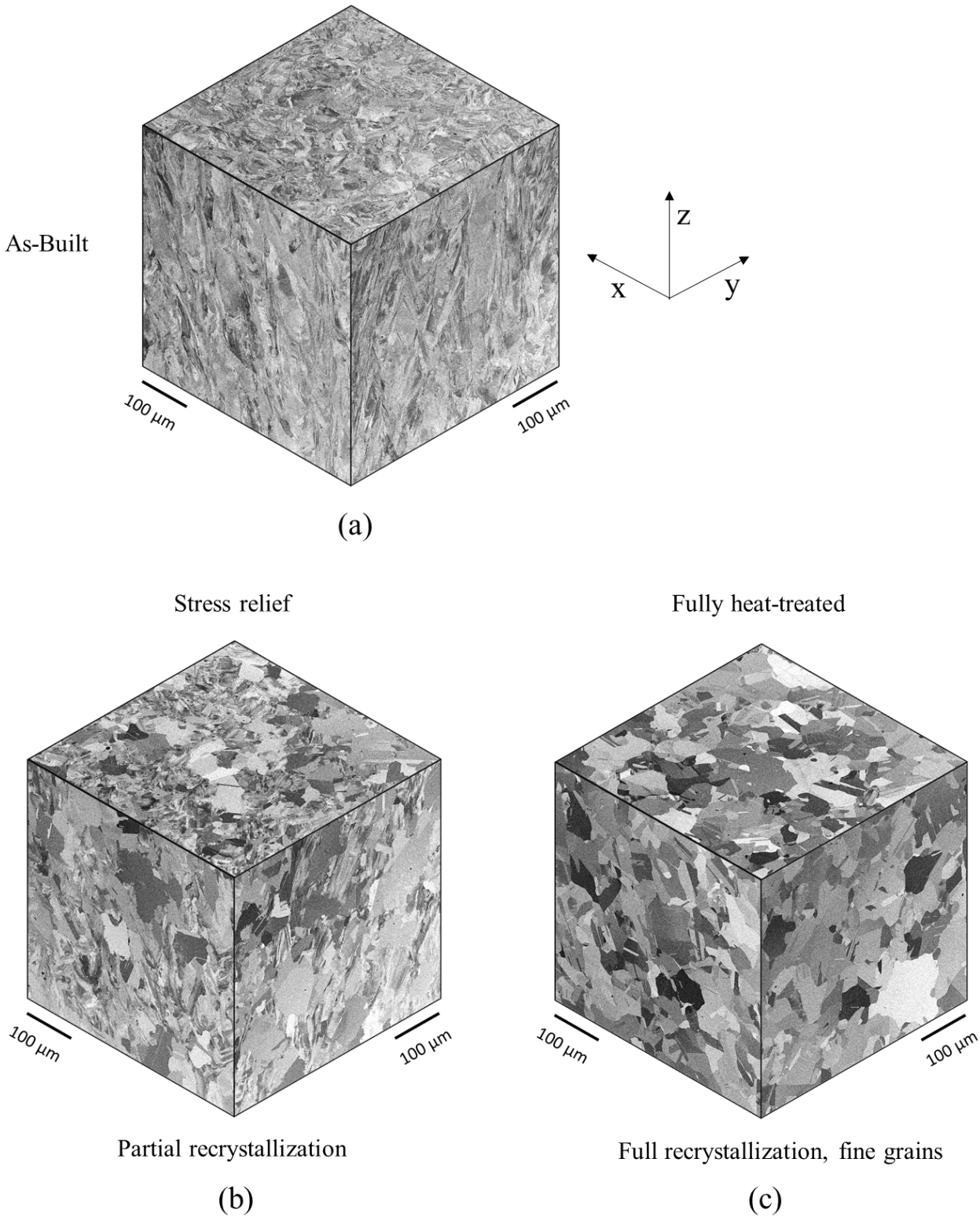


**Figure 21.** Quasi-3D images showing microstructure evolution of B-4 samples before and after post-processing heat treatment (formulation II).

### 4.7 Temperature-Dependent Tensile Properties in Ambient Air

Temperature-dependent tensile properties of L-PBF NASA HR-2 were investigated using fully heat-treated samples. L-PBF NASA HR-2 round bar was machined into a cylindrical-shaped tensile specimen along the build direction with a gauge length of 0.75 inch and 0.188 inch in diameter. **Table 4** summarizes the tensile properties of L-PBF NASA HR-2 as a function of testing temperature at –423 °F, –320 °F, room temperature, and 1,200 °F. It can be seen from **Table 4** that both YS and UTS decrease with an increase in the test temperature from –423°F to 1,200 °F.

UTS/YS ratio also decreases when the test temperature increases. UTS/YS ratios correlate well with strain hardening exponent and can be used to estimate static strain hardening capability **[7, 42]**. Tensile fracture elongation is very high (around 37–42% in cryogenic temperatures), and it decreases slightly to 34–38% at room temperature. A significant reduction in fracture elongation was noted when the testing temperature is increased to 1,200 °F, which hints a change in the deformation mechanism.

**Table 4.** Summary of tensile properties of L-PBF NASA HR-2 at four different temperatures.

| Material | Test Environment | Composition | Yield Stress (ksi) | Ultimate Tensile Stress (UTS) | Fracture Elongation (%) | UTS/YS Ratio |
|---|---|---|---|---|---|---|
| L-PBF NASA HR-2 | $LH_2$, –423 °F | Formulation II | 134.19 | 244.33 | 37.65 | 1.82 |
| | $LN_2$, –320 °F | Formulation I | 130.46 | 225.61 | 39.2 | 1.73 |
| | | Formulation II | 114.31 | 215.15 | 41.91 | 1.88 |
| | Air, RT | Formulation I | 105.24 | 165.74 | 34.76 | 1.57 |
| | | Formulation II | 93.89 | 167.21 | 37.65 | 1.78 |
| | Air, 1,200 °F | Formulation I | 93.56 | 125.9 | 20.18 | 1.35 |
| | | Formulation II | 85.36 | 121.68 | 16.93 | 1.43 |

It is significant to note that tensile testing at cryogenic temperatures for L-PBF NASA HR-2 shows a significant enhancement in both strength and ductility. Materials with FCC crystal structure, such as NASA HR-2, are well-suited for cryogenic applications as they have 12 available dislocation slip systems that can assist in absorbing plastic deformation in extremely cold conditions. Many FCC alloys exhibit greater strain hardening capability at cryogenic temperature because the reduced internal energy of atoms impedes the movement of dislocations **[7]**. Tensile fracture elongation is typically proportional to the value of strain hardening exponent (n) as high strain hardening capability can homogenize plastic deformation and retard tensile

fracture initiation (necking). Therefore, the improved ductility in cryogenic temperatures can be attributed to the enhanced strain hardening capability (higher UTS/YS ratio) that increases the material's ability to absorb plastic deformation and makes deformation more homogeneous and stable prior to fracture.

### 4.7.1 L-PBF NASA HR-2 and LP-DED NASA HR-1 Comparison

The tensile properties of L-PBF NASA HR-2 obtained from this study are compared with literature data for LP-DED NASA HR-1 **[7]** and presented in **Figure 22**. Overall, the temperature-dependent trends in tensile behavior are similar between the two alloys. L-PBF NASA HR-2 has higher strength but lower fracture elongation than LP-DED NASA HR-1 under the same test temperatures. Compared with LP-DED NASA HR-1, the ultimate tensile stress of L-PBF NASA HR-2 (formulation II) increases from 202.0 to 225.6 ksi at –320 °F, from 154.0 to 165.8 ksi at room temperature, and from 110.0 to 122.9 ksi at 1,200 °F. Although strength decreases with increasing temperature, both yield and tensile strengths remain stable up to 1,200 °F. Compared with LP-DED NASA HR-1, the ductility of L-PBF NASA HR-2 (formulation II) decreases from 49% to 41.9% at –320 °F, from 41% to 31.7% at room temperature, and from 27% to 16.94% at 1,200 °F. Overall, L-PBF NASA HR-2 has slightly lower fracture elongation than LP-DED NASA HR-1, but it is significantly more ductile than most commercial Ni-based and Fe-Ni-based superalloys. L-PBF NASA HR-2 is specifically designed as an L-PBF solution to fabricate hydrogen-sensitive components for LRE applications. L-PBF NASA HR-2 is also an excellent material for use in extremely cold conditions. L-PBF NASA HR-2 exhibits very high UTS of 225.6 ksi and more than 41.0% in fracture elongation at –320 °F, which can be attributed to its enhanced strain hardening capability (higher UTS/YS ratio) at cryogenic temperatures.

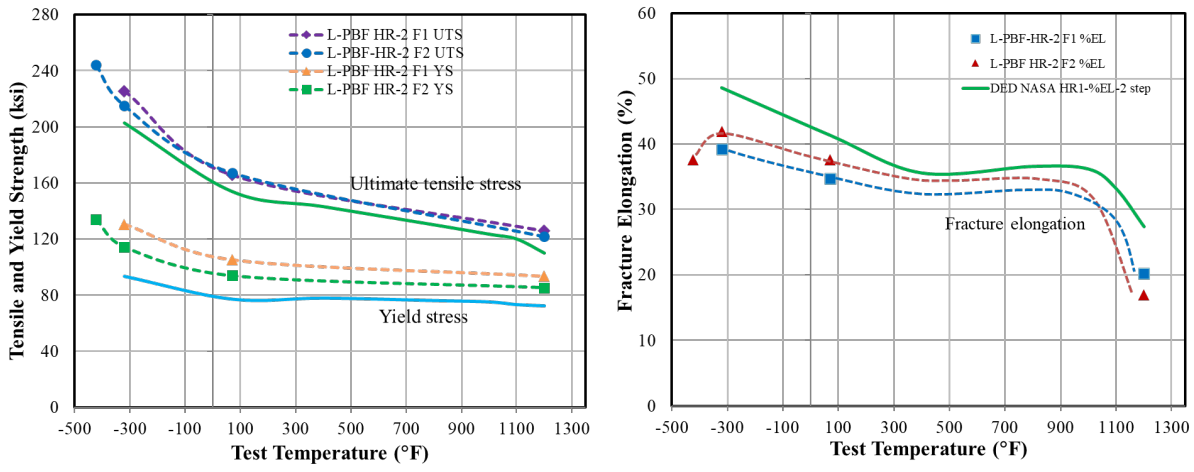


(a) (b)

**Figure 22.** The tensile properties of L-PBF NASA HR-2 obtained from this study are compared with those reported for LP-DED NASA HR-1 in the literature **[7]**.

### 4.7.2 L-PBF NASA HR-2 and Wrought A-286 Comparison

The cryogenic tensile properties of L-PBF NASA HR-2 from this study are compared with those of wrought A-286 data reported in the literature **[44]** and presented in **Figure 23**. Temperatures of –320 and –423 °F were obtained with the specimens submerged in $LN_2$ and $LH_2$, respectively. As shown, both yield and tensile strengths increase rapidly with decreasing temperature. In contrast, fracture elongation increases notably at –320 F but decreases slightly at –423 °F. Overall, the enhancement in cryogenic tensile properties followed a similar trend for both alloys. L-PBF NASA HR-2 has significantly higher UTS and fracture elongation than wrought A-286 but slightly lower yield stress. At cryogenic temperatures, the strengths and elongation are improved over the room-temperature values for both alloys. The cryogenic tensile behavior of L-PBF NASA HR-2 is unique in its remarkable enhancement in yield and ultimate tensile strengths. One notable difference between L-PBF NASA HR-2 and A-286 is that L-PBF NASA HR-2 exhibits a more pronounced increase in both yield and ultimate tensile strengths than wrought A-286 at –423 °F (over the values at –320 °F).

Both alloys exhibit increased fracture elongation at –320 °F compared to room temperature. But their ductility drops slightly when the test temperature is further decreased from –320 °F to 423 °F. Overall, the fracture elongation of L-PBF NASA HR-2 is very high at 423 °F (37%) and remains comparable to that at room temperature. The slight reduction in fracture elongation at –423 °F can be attributed to the reduction of UTS/YS ratio (from 1.88 at –320 °F to 1.81 at –423 °F), which is likely caused by the drastic increase in yield strength from 114 ksi (at –320 °F) to 135 ksi (at –423 °F). The enhanced tensile performance of L-PBF NASA HR-2 at cryogenic temperatures results from a change in the plastic deformation mechanism from predominant dislocation slip at room temperature to deformation twinning at cryogenic temperatures **[45–50]**. When L-PBF NASA HR-2 is tensile-tested at cryogenic temperatures, numerous deformation twins form, and the yield strength increases significantly as twins act as strong barriers to mobile dislocations. In addition, the profuse formation of deformation twins at cryogenic temperature led to a higher strain hardening effect that contributes to improved fracture elongation. Overall, L-PBF NASA HR-2 alloy shows an excellent balance of strength and ductility at cryogenic temperatures. The 0.2% yield stress and the UTS of this alloy increased significantly in an extremely cold condition with no loss of fracture elongation. These properties make L-PBF NASA HR-2 a highly promising material for fabricating hydrogen-fueled LRE components that operate in extremely cold conditions below –320 °F.

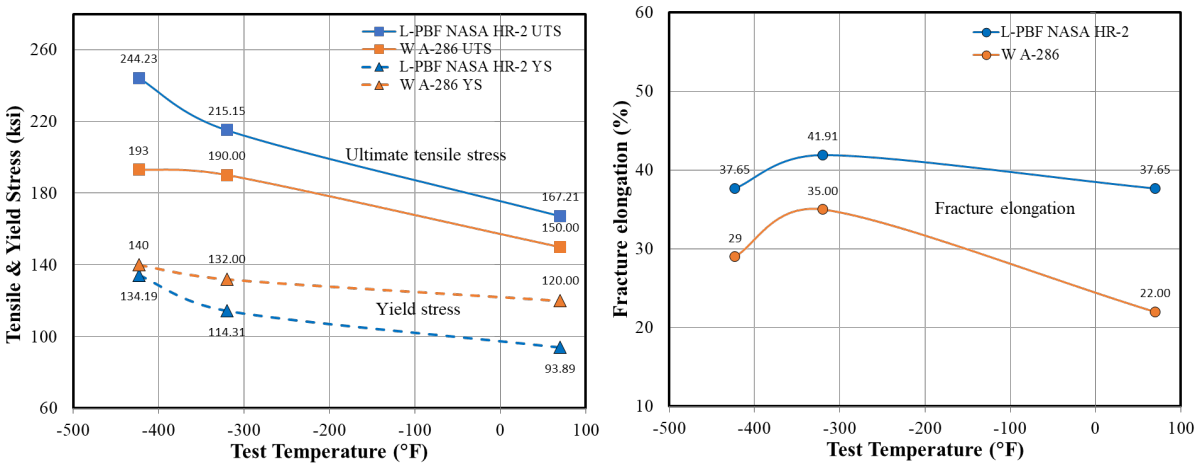


**Figure 23.** Cryogenic tensile properties of L-PBF NASA HR-2 obtained in this study compared to the A-286 data reported in the literature **[44]**: (a) tensile and yield strengths and (b) fracture elongation.

### 4.7.3 Deformation and Fracture Behavior at Elevated Temperature

The crystal lattice expands at elevated temperatures, and dislocation motion becomes easier. As a result, the degree of strain hardening is considerably reduced by a lower UTS/YS ratio. Slip lines also become more widely spaced after tensile testing at elevated temperatures. Optical microscopy and SEM were performed to observe deformation-induced microstructure evolution near the fracture surface.

As shown in **Figure 24**, tensile deformation at 1,200 °F results in isolated grain boundary cracking near the fracture surface. This suggests that ductility reduction at 1,200 °F is caused by a change in fracture mode from transgranular to partial intergranular fracture. While grain boundaries provide strengthening effects at lower temperatures, they become weaker than the matrix at elevated temperatures. Consequently, plastic deformation occurs through a combination of dislocation slip and grain boundary sliding, leading to the formation of cracks along grain boundaries, as shown in **Figure** 24. Based on these findings, L-PBF NASA HR-2 is recommended for component applications up to 1,200 °F.

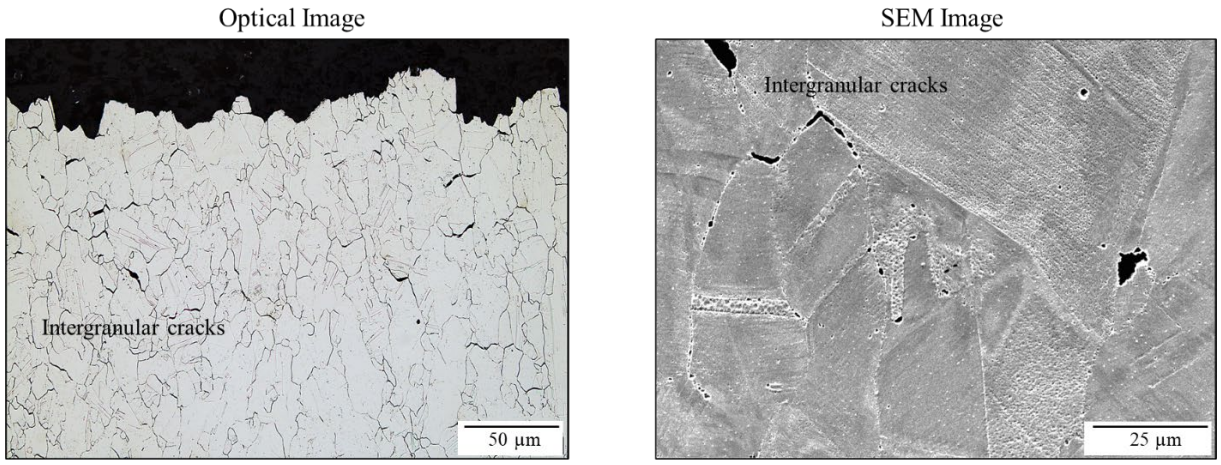


**Figure 24**. Cross-sectional views of the fractured tensile samples after testing at 1,200 °F.

Figure 25 presents the fracture surface morphologies of L-PBF NASA HR-2 after tensile testing at 1,200 °F. The fracture surface exhibits a predominantly ductile transgranular fracture mode, with several small partial intergranular fracture zones observed near the specimen gauge surface.

These isolated intergranular zones are associated with the observed reduction in ductility—from 34–38% at room temperature to 17–20% at 1,200 °F. This decline is likely due to grain boundaries becoming the weakest link in the microstructure when the temperature exceeds 0.5 Tm, approximately 1,250 °F for L-PBF NASA HR-2 **[43]**.

At elevated temperatures, plastic deformation proceeds via a combination of dislocation slip and grain boundary sliding, particularly when grain boundaries are weaker than the grain interiors. The presence of partial intergranular fracture zones thus indicates that grain boundary sliding became more prominent at 1,200 °F, leading to crack formation along grain boundaries, as shown in Figure 25.

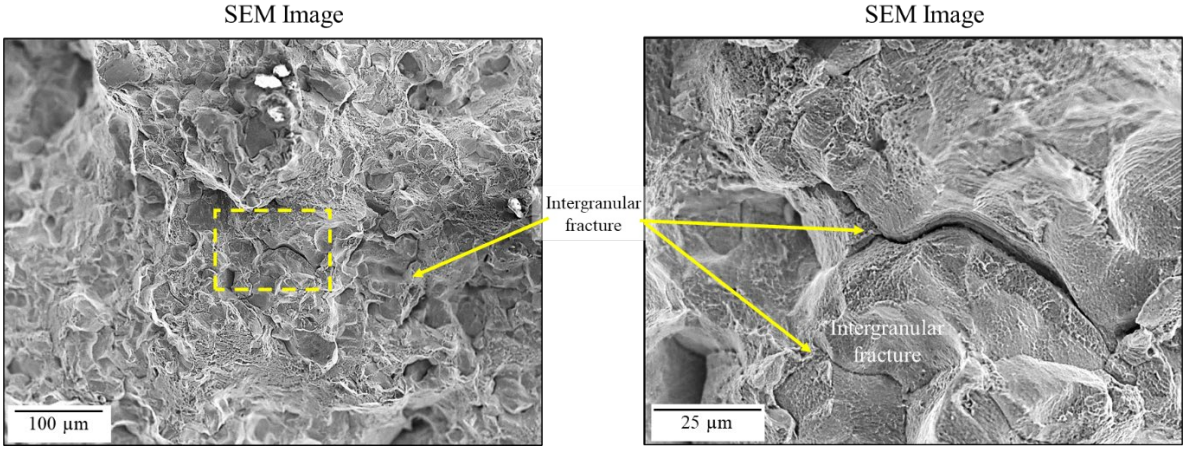


**Figure 25.** Fracture surfaces of L-PBF NASA HR-2 tensile tested at 1,200 °F. Some isolated partial intergranular fracture zones are present near the specimen gauge surface. Ductile dimple type of fracture predominates away from the specimen gauge surface.

### 4.7.4 Deformation and Fracture Behavior at Cryogenic Temperatures

An in-depth analysis on tensile deformation and fracture behavior was performed to elucidate the mechanisms responsible for the drastic improvement in tensile properties at cryogenic temperatures. Fractography revealed the presence of fine, submicron-sized dimples (< 2 μm) on the fracture surface of specimens tested from room temperature to –423 °F, as shown in **Figure 26**. These features are characteristic of ductile transgranular fracture resulting from the nucleation, growth, and coalescence of voids. Although all three specimens (tested at three different temperatures) exhibited predominantly ductile dimple rupture, the dimple size decreased with decreasing temperature. As illustrated in **Figure 26 (c), (f),** and **(i)**, the dimples observed in the specimens tested at cryogenic temperatures are clearly smaller and shallower than those tested at room temperature. In addition, the dimples in the specimens tested at cryogenic temperatures appear more elongated or drawn out along one direction, which is a typical feature of shear fracture. It is evident that shear-dominated fracture mechanism becomes more prevailing during tensile testing at –320 °F and –423 °F, causing the dimples to align at an angle along the shear direction.

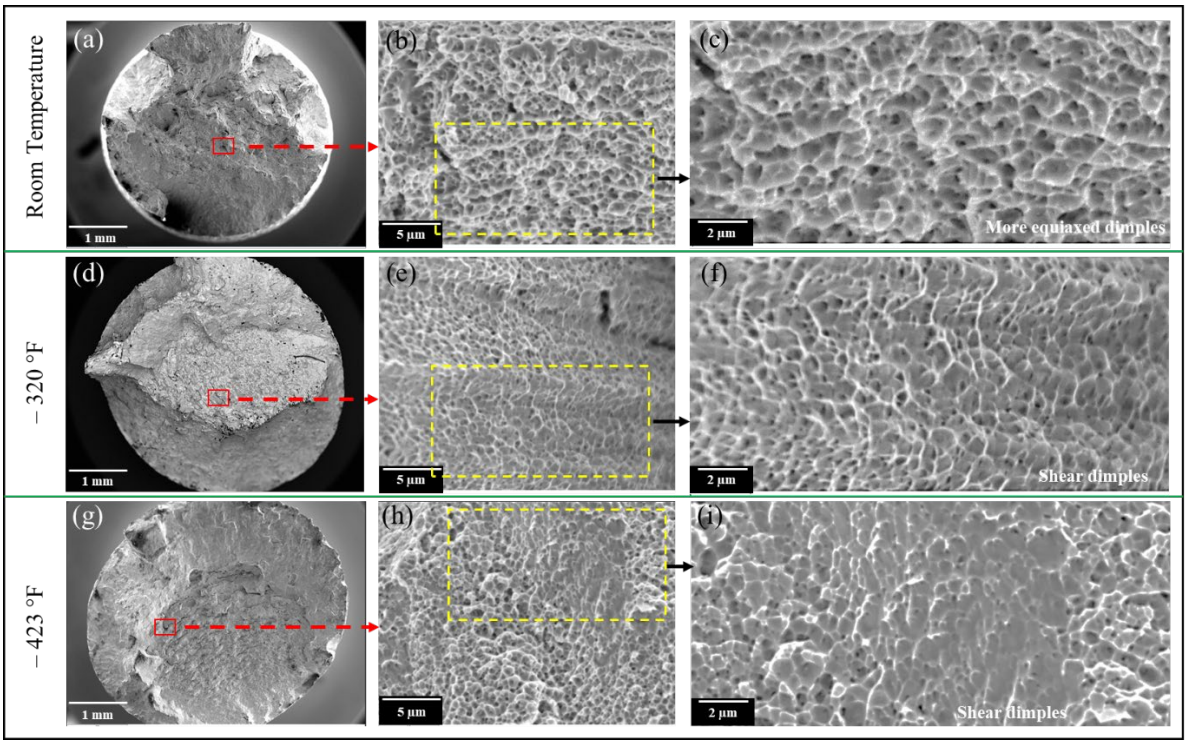


**Figure 26.** Fractography of L-PBF NASA HR-2 specimens tested at (a)–(c) room temperature, (d)–(f) –320°F, and (g)–(i) –423°F. The dimples in the specimens tested at cryogenic temperatures appear more shallow and more elongated, which are the typical features arising from a shear fracture.

It is well documented that deformation twinning becomes the dominant deformation mechanism under cryogenic conditions in Ni-based superalloys **[45–50]**. This is primarily because the dislocation slip is a thermally activated process and requires very high stress to activate under extremely cold conditions. In contrast, the activation of twinning is relatively insensitive to the testing temperature, making twinning the predominant mechanism of plastic deformation at cryogenic temperatures **[45–50]**. Features indicative of deformation twinning were found on the fracture surfaces of the specimen tensile tested at –423 °F. Fine striations were observed on the fracture surface as shown in **Figure 27(a)**. Fine dimples interconnected between the striations (see **Fig. 27(b)** and **(c)**) represent a unique fracture characteristic not observed in the specimen tensile tested at room temperature. The dimples between the striations are clearly elongated along a single direction in between striations, suggesting the formation of striations resulted from shear-dominated deformation events. Similar features—striations accompanied by elongated shear dimples—were also observed in the specimen tensile tested at –320 °F, as shown in **Figure 28**, although the striations are more widely spaced and the dimples slightly larger.

The appearance of parallel striations with sub–0.5 μm spacing on the fracture surfaces, as shown in **Figure 27**, suggests mechanical twinning likely emerged as a key deformation mechanism during tensile testing at cryogenic temperatures and strongly influenced the fracture characteristics. The tightly spaced striations, shown in **Figure 27(c)**, may correspond to deformation twin boundaries, which can hinder dislocation motion as the growth of shear dimples terminates at striation interfaces. The variation in striation spacing between the specimens tested at –320 °F and –423 °F can be attributed to differences in the testing temperature. In superalloy 625, it has been observed that the thickness of deformation twins decreases with decreasing test temperature due to reduced stacking fault energy when the temperature drops **[51]**. Accordingly, the spacing between striations is finer in the specimen tested in $LH_2$ (–423 °F) than that tested in $LN_2$ (–320 °F). Further confirmation of deformation twinning as the predominant deformation mechanism at cryogenic temperatures for L-PBF NASA HR-2 will be provided through microstructure analysis adjacent to the fracture surface.

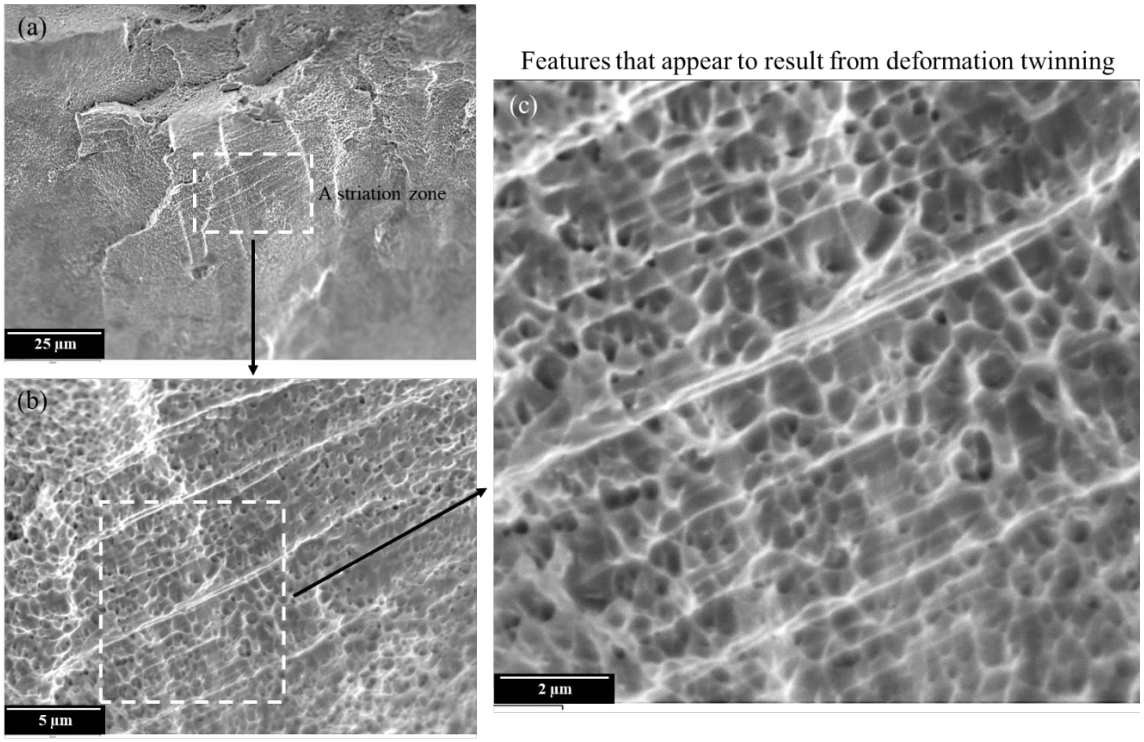


**Figure 27.** Fractography of L-PBF NASA HR-2 specimens tested at –423 °F. Note the voids are interconnected laterally just beneath the fracture striations.

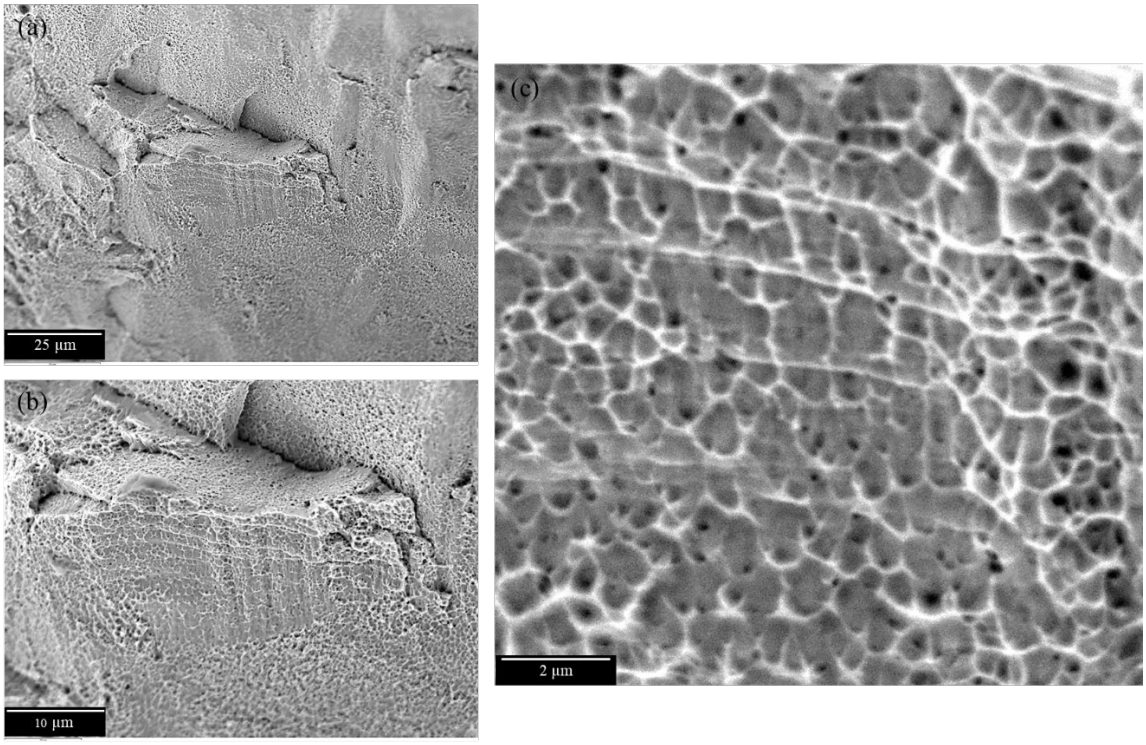


**Figure 28.** Fractography of L-PBF NASA HR-2 specimens tested at –320° F. Note the voids are interconnected laterally just beneath the fracture striations.

To further understand the deformation mechanisms in cryogenic temperatures, the microstructure beneath the fracture surface of broken tensile specimens was analyzed using SEM. **Figure 29** presents a representative microstructure adjacent to the fracture surface of a tensile specimen tested in $LN_2$. As shown, deformation twinning had occurred at cryogenic temperatures as many fine deformation twins are present adjacent to the fracture surface. These observations confirmed that deformation twinning had played a vital role in contributing to the drastic enhancement in strength from 167.21 ksi at room temperature to 215.15 ksi in $LN_2$, and 244.23 ksi in $LH_2$, while maintaining excellent ductility of >37% in fracture elongation under extremely cold conditions (–320 °F and –423 °F). At cryogenic temperatures, the critical resolved shear stress for dislocation slip increases significantly, while the stress required for deformation twinning remains relatively unchanged, making twinning the dominant deformation mechanism **[45–50]**. Under this circumstance, twinning-induced plasticity led to the formation of finely spaced striations on the fracture surface as shown in **Figure 27** and **Figure 28**. The presence of micro-twins with width below 0.5 µm confirms the tightly spaced striations observed on the fracture surface, as shown in **Figure 27 and Figure 28**, are boundaries of deformation twins.

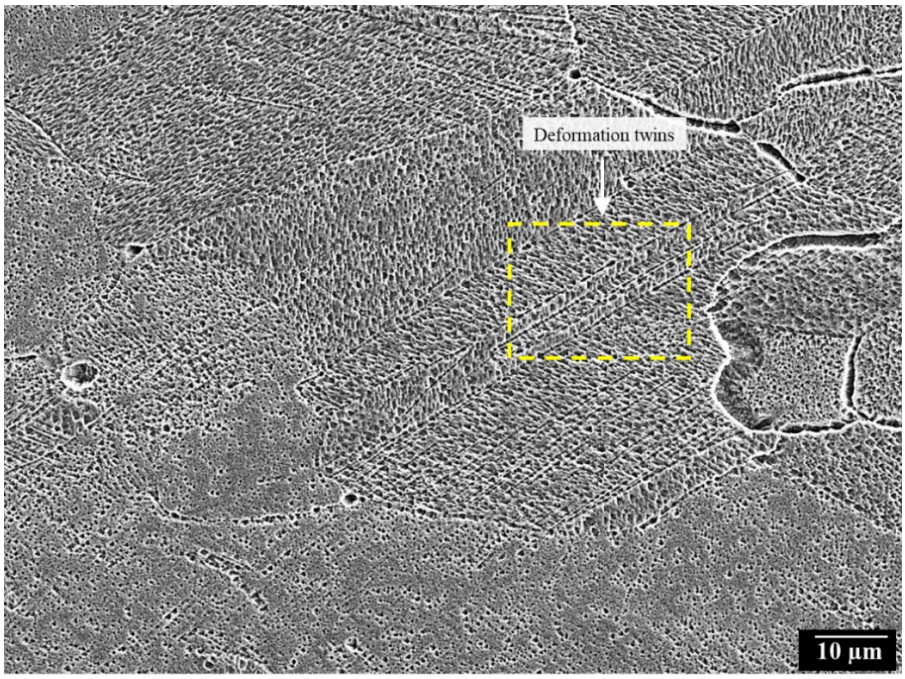


(a)

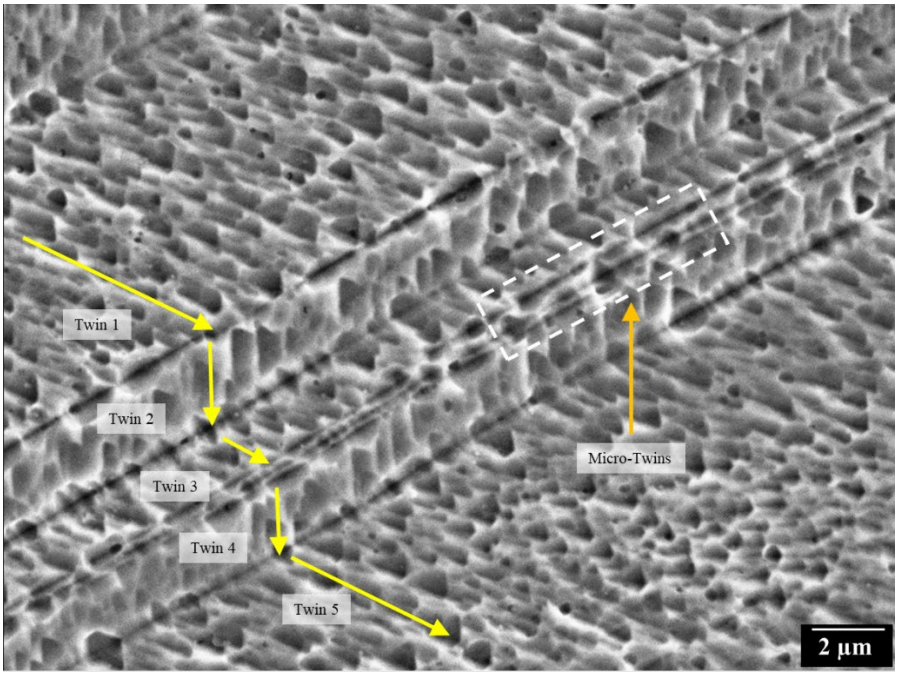


(b)

**Figure 29.** (a) SEM images showing deformation twinning were activated in the tensile specimen tested at –320°F. (b) Close-up view of the yellow box in (a). The stepped appearance and layered morphology suggest classic mechanical twinning behavior. The yellow arrows

represent the change in microstructure flow direction due to the occurrence of deformation twinning.

### 4.8 Tensile Properties in High-Pressure Hydrogen Environment

As an initial material screening to assess the susceptibility of HEE, tensile testing was conducted for L-PBF NASA HR-2 in a 5-ksi high-pressure $GH_2$ environment at ambient temperature. The term "HEE" refers to the degradation of certain mechanical properties when the material is exposed to a high-pressure $GH_2$ environment, relative to the performance in an inert environment **[52]**. HEE susceptibility is known to be temperature-dependent, with the greatest effect usually occurring near room temperature. The tensile ductility degradation of smooth tensile specimens, tested in hydrogen versus that in an inert environment, is commonly used to evaluate HEE susceptibility **[52]**. **Figure 30** shows the microstructure (in X-Z plane) of L-PBF NASA HR-2 samples prior to tensile testing in hydrogen. **Table 5** summarizes the tensile properties for L-PBF NASA HR-2 tested in 5-ksi $GH_2$ environment at room temperature. All specimens exceed the 15% strain limit of the calibrated extensometer. Effective elongation is calculated from the initial specimen length, final fit-back length, and nominal gage length. As expected, hydrogen exposure has insignificant influence on the tensile properties of L-PBF NASA HR-2. Formulation I material exhibits slightly higher YS but lower UTS and ductility than the formulation II samples. Tensile ductility in hydrogen, as represented by total fracture elongation, ranges from 33.06–34.80% for formulation I and from 36.13–37.06% for formulation II. It is significant to note that tensile ductility in hydrogen remains quite high for both formulations and comparable to that measured in ambient air (see **Table 5**).

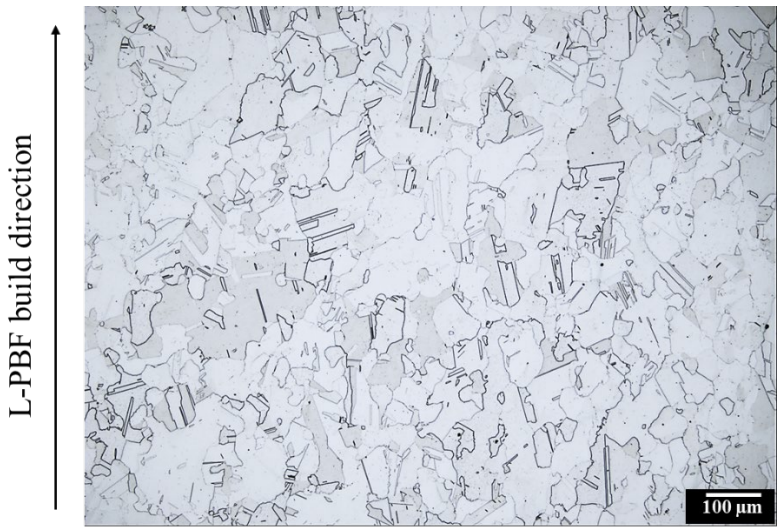


**Figure 30.** The typical microstructure (in X-Z plane) of L-PBF NASA HR-2 specimen used for tensile testing in 5-ksi $GH_2$ environment. The average grain size is approximately 75 µm.

**Table 5.** Tensile properties for L-PBF NASA HR-2 for the tests performed in 5-ksi high-pressure hydrogen environment.

| Material | Strain rate (in/in/min) | Test Environment | Composition | Specimen ID # | Yield Stress (ksi) | Ultimate Tensile Stress (UTS) | Modulus of Elasticity (MSI)* | Fracture Elongation (%) |
|---|---|---|---|---|---|---|---|---|
| L-PBF NASA HR-2 (B-4) | 0.005 | 5 ksi $GH_2$, RT | Formulation I | 1-2 | 95.52 | 162.72 | 28.45 | 33.06 |
| | | | | 1-6 | 97.59 | 164.76 | 29.45 | 34.80 |
| | | | | 1-5 | 95.76 | 164.69 | 27.36 | 34.00 |
| | | | Formulation II | 2-2 | 90.99 | 166.06 | 24.86 | 37.06 |
| | | | | 2-3 | 91.82 | 165.57 | 26.73 | 36.13 |
| | | | | 2-6 | 92.03 | 166.23 | 26.00 | 36.53 |

* Modulus of elasticity value is for reference only. Specific modulus tests are required for true value.

The ratios of YS, UTS, and ductility (fracture elongation) for L-PBF NASA HR-2 tested in high-pressure hydrogen versus air are given in **Table 6**. The most significant effects of high-pressure hydrogen environments are typically observed in tensile ductility, notch tensile strength, and crack behavior **[20]**. In contrast, the elastic properties and tensile yield strengths of metals in hydrogen are generally comparable to those measured in air or inert environments **[2, 6]**. As shown in **Table 6**, the YS ratio for formulation I is unusually low, which likely results from the higher-than-expected modulus of elasticity and yield stress in the air-tested samples. Abnormally high modulus of elasticity can occur due to the use of an incorrect type of extensometer. Because tensile tests are not optimized for precise modulus measurement, the reported modulus of elasticity should be considered approximate; accurate determination requires dedicated modulus testing.

It is significant to note that hydrogen has a negligible effect on the UTS as the UTS ratios ($GH_2$/air) for LP-DED NASA HR-2 are above 99%. This finding indicates that hydrogen had little effect on the stress required to initiate plastic deformation. In general, the primary effect of hydrogen is, in general, on plastic deformation and ductility. Tensile ductility ratios ($GH_2$/air) are widely used to assess a material's susceptibility to HEE. L-PBF NASA HR-2 exhibits only a slight reduction in tensile ductility in hydrogen with ductility ratios ($GH_2$/air) around 97 to 98% for both formulations, as illustrated in **Figure 31**. Although L-PBF NASA HR-2 shows very high $GH_2$/air tensile ductility ratio, tensile properties in hydrogen are intended for initial material screening and should not be used for component design. Further mechanical testing in high-pressure hydrogen environments is needed to evaluate the effects of hydrogen on other critical mechanical properties such as LCF, HCF, and fatigue crack growth.

**Table 6.** The $GH_2$/air ratios of YS, UTS, and ductility (fracture elongation) for L-PBF NASA HR-2.

| Material | Strain rate (in/in/min) | Composition | YS Ratio ($GH_2$/Air) | UTS Ratio ($GH_2$/Air) | Ductility Ratio ($GH_2$/Air) |
|---|---|---|---|---|---|
| L-PBF NASA HR-2 (B-4) | 0.005 | Formulation I | 0.92 | 0.99 | 0.98 |
| | | Formulation II | 0.98 | 0.99 | 0.97 |

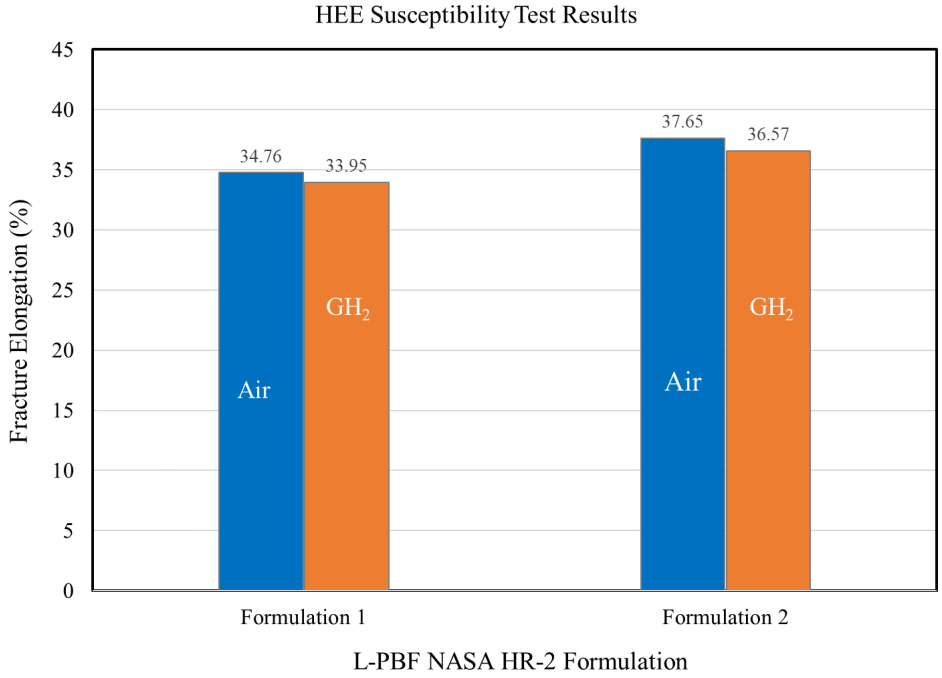


**Figure 31.** HEE susceptibility comparison for L-PBF NASA HR-2 formulation I and II (B-4 parameter). Both formulations show a slight reduction in tensile fracture elongation when testing in a 5-ksi $GH_2$ environment verses that in ambient air.

Alloys A-286 and JBK-75 are well-established HEE-resistant Fe-Ni-based superalloys that are commonly used for hydrogen-sensitive components of the RS-25 rocket engine. A comparison of tensile properties in hydrogen for wrought A-286, wrought JBK-75, and L-PBF NASA HR-2 is shown in **Figure 32**. All three alloys have excellent resistance to HEE, showing negligible degradation in UTS and ductility in hydrogen. Compared to the wrought A-286 and JBK-75 alloys, L-PBF NASA HR-2 exhibits comparable UTS but significantly higher ductility (fracture elongation) in hydrogen, as shown in **Figure 32**. The most outstanding attribute of L-PBF NASA HR-2 is its ability to achieve tensile strength exceeding 165 ksi (1,210 Mpa), while maintaining higher than 34% fracture elongation in hydrogen. Wrought A-286 and JBK-75 also have excellent resistance to HEE, but they are not as ductile as L-PBF NASA HR-2, exhibiting lower fracture elongation values in the range of 22–23% under the same hydrogen testing conditions.

Although A-286 and JBK-75 have excellent resistance to HEE, both alloys have limitations as they cannot be readily built using L-PBF. A-286 has poor weldability, and JBK-75 is highly susceptible to hot cracking during the L-PBF process **[9,10]**. In contrast, NASA HR-2 was specifically developed as an AM solution for fabricating hydrogen-sensitive LRE components that require strong resistance to HEE. NASA HR-2 demonstrates excellent 3D printability and is

currently the only HEE-resistant superalloy that can be successfully processed via the L-PBF technique.

The use of L-PBF opens new design and manufacturing opportunities for NASA HR-2, enabling the fabrication of hydrogen-sensitive components with complex geometries and fine feature resolution. L-PBF NASA HR-2 is currently being demonstrated in various LRE components, targeting hydrogen-fueled turbopumps in the RS-25 engine as a potential replacement for forged and cast A-286 and JBK-75 parts.

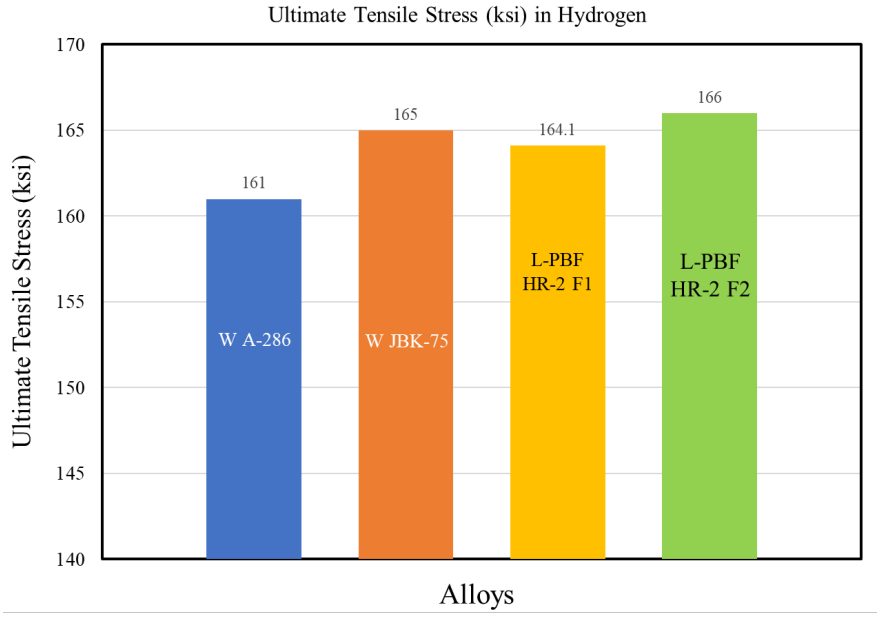

(a)

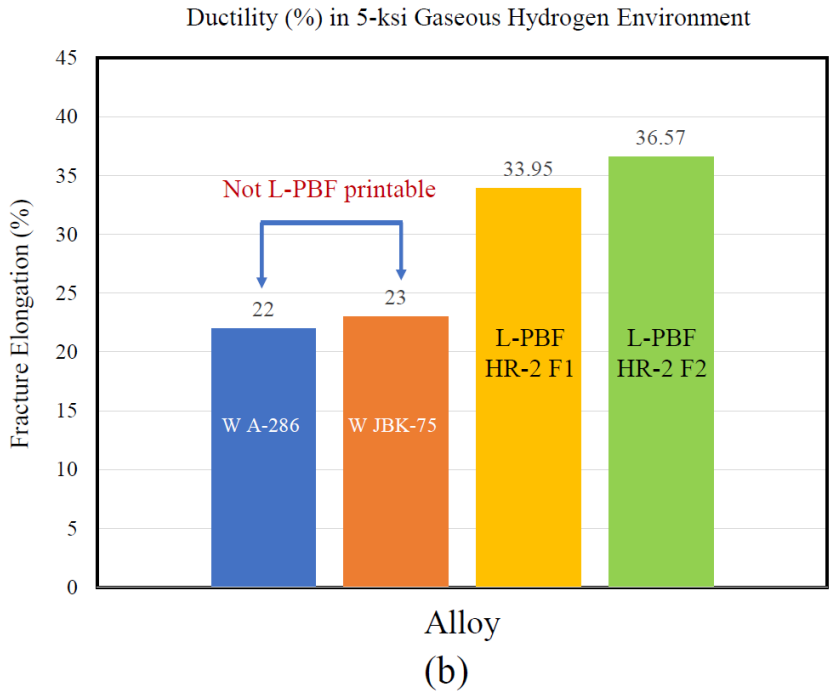


**Figure 32.** Comparison of (a) ultimate tensile stress and (b) tensile fracture elongation in hydrogen for wrought A-286, wrought JBK-75, and L-PBF NASA HR-2. A-286 and JBK-75 are not printable via L-PBF due to their susceptibility to hot cracking. L-PBF NASA HR-2 (B-4 parameter) exhibits comparable ultimate tensile stress but significantly higher fracture elongation than wrought A-286 and JBK-75 in hydrogen.

### 4.8.1 Hydrogen-Induced Surface Cracking

The tensile behavior of metals in hydrogen differs significantly from that in air. The primary effect of high-pressure $GH_2$ exposure on metals is surface embrittlement. Surface cracks form as the material loses its ability to accommodate tensile plastic deformation in hydrogen to the same degree as it can in air or inert environments. When a hydrogen-susceptible metal is stressed in tension in hydrogen to a critical amount of plastic deformation, surface cracks form. The deformed surfaces of tensile-tested specimens were examined with SEM to analyze the hydrogen-induced surface cracking behavior.

**Figure 33** illustrates the surface characteristics of formulation 1 and formulation 2 specimens after tensile testing in hydrogen. The images clearly show that tensile plastic deformation in hydrogen results in surface cracking. The presence of surface cracks is indicative of hydrogen-induced or hydrogen-assisted cracking that becomes more pronounced after macroscopic necking **[53]**. Surface cracks became wider and longer near the fracture surface, consistent with the development of a triaxial stress state during necking [**54**].

As shown in **Figure 33**, surface cracks on both specimens are very shallow and randomly orientated. In general, more pronounced surface cracking corresponds to a greater susceptibility

to HEE. The presence of very fine and shallow surface cracks on the specimen surface suggests L-PBF NASA HR-2 has low susceptibility to HEE.

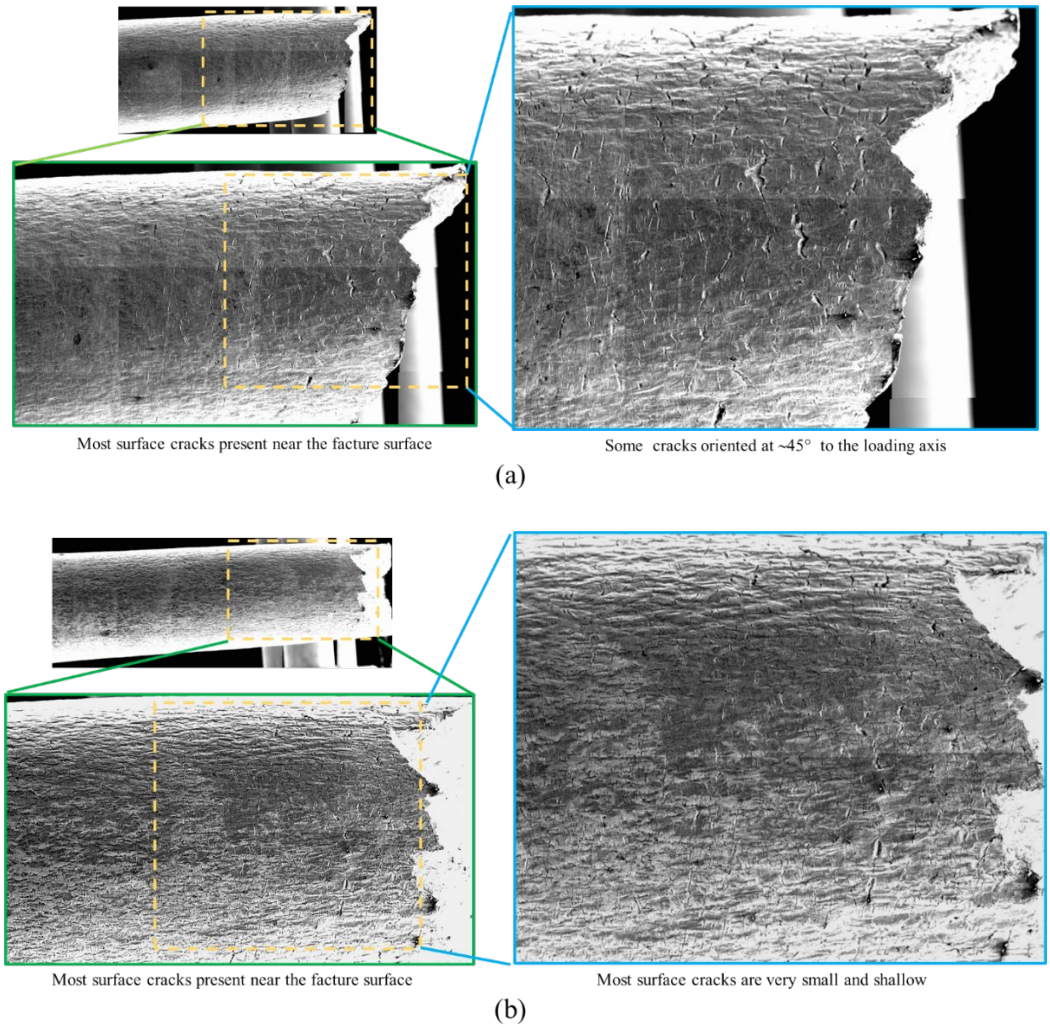


**Figure 33.** SEM images showing surface cracking behavior of (a) formulation I and (b) formulation II L-PBF NASA HR-2 samples tensile-tested in hydrogen. Three images are presented for each sample to illustrate surface cracking features.

### 4.8.2 Depth of Surface Crack Analysis

An in-depth analysis of the deformed microstructure and surface cracks was performed to assess the effects of hydrogen exposure, as shown in **Figure 34**. Both formulation I and II samples display similar surface cracking characteristics after tensile testing in hydrogen. The fracture surface is inclined at approximately 45° to the tensile loading direction, aligning with the plane of near maximum shear stress. Many surface cracks also formed at an inclination of approximately 45° to the loading axis, and most of them are 20–60 μm deep.

The surface cracking mode is predominantly ductile transgranular, indicating that the L-PBF NASA HR-2 alloy retains significant ductility even in a hydrogen environment. Crack initiation

via a ductile shear mechanism suggests that hydrogen exposure did not fundamentally alter the alloy's ductile failure behavior. The fracture surfaces showed classic characteristics of ductile transgranular failure, with no signs of hydrogen-induced brittle intergranular fracture. These findings indicate that L-PBF NASA HR-2 exhibits low susceptibility to hydrogen embrittlement and retains its mechanical integrity in hydrogen-rich environments.

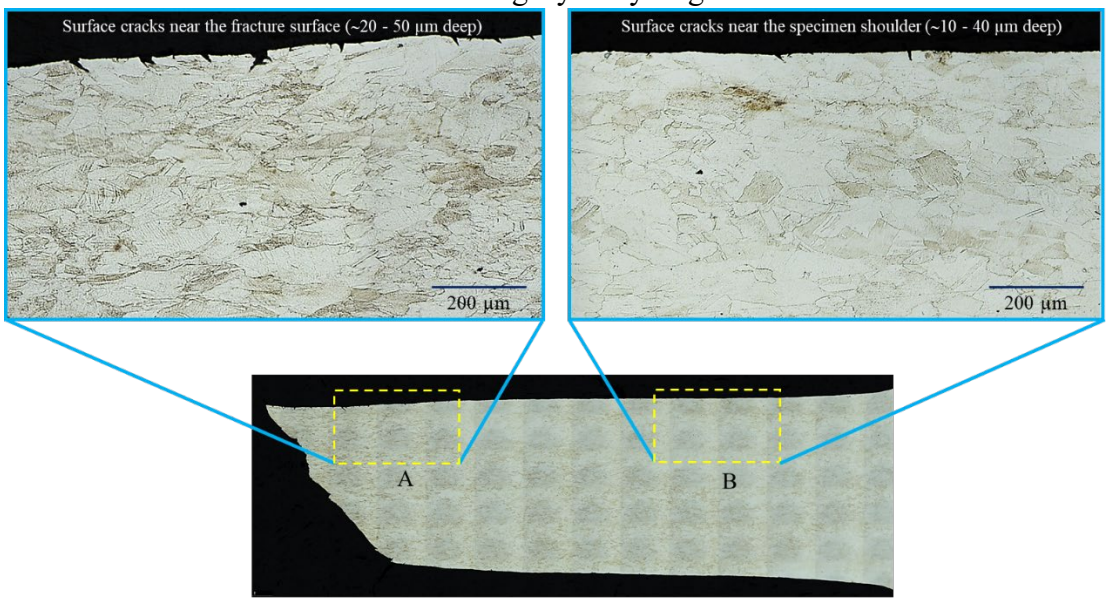


(a)

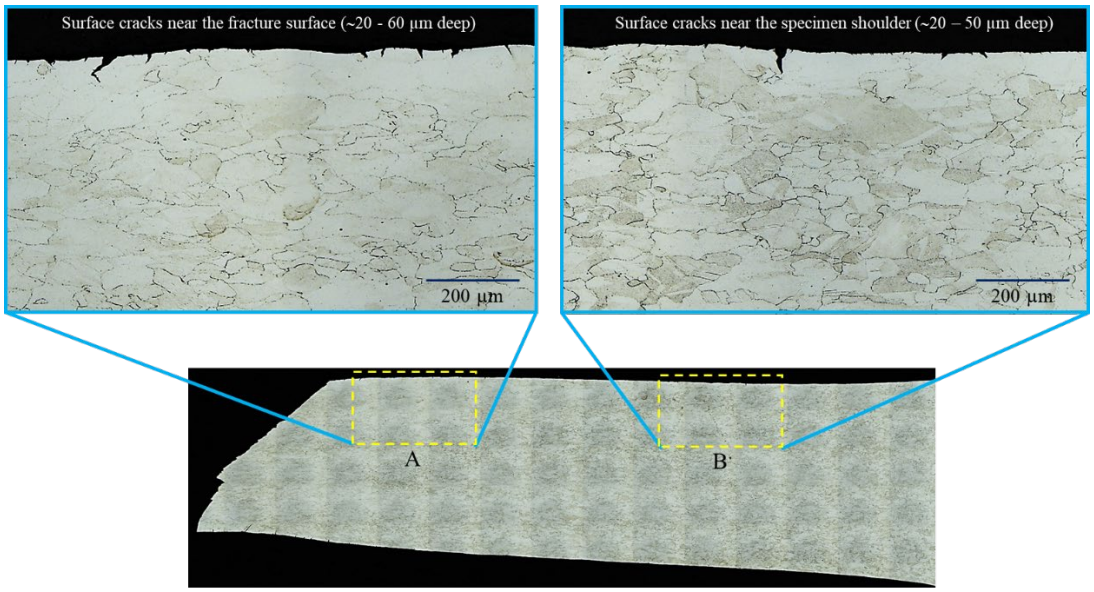


(b)

**Figure 34.** Optical images showing cross-section of fractured tensile samples tested in 5-ksi $GH_2$. Surface cracks formed at an inclination of approximately 45° angle to the loading axis.

### 4.8.3 Effects of Hydrogen on Fracture Behavior

Fracture surfaces were analyzed using SEM to assess the effects of hydrogen on the tensile fracture behavior of L-PBF NASA HR-2. Fractographic details for a formulation II specimen are shown in **Figure 35**. Three images are presented, including one showing the HAZ near the surface and two higher resolution images illustrating mixed quasi-cleavage and ductile dimple fracture in the HAZ. As shown in **Figure 35**, the interaction of $GH_2$ with the tensile specimen is confined to the outer region of the fracture surface. A very small HAZ is observed around the circumference of the fracture surface. High resolution SEM images reveal that this zone is characterized predominantly by ductile dimple fracture, with occasional, very fine quasi-cleavage cracks indicative of limited hydrogen-induced embrittlement. These observations suggest that hydrogen exposure has minimal influence on the overall tensile fracture behavior of L-PBF NASA HR-2. The fracture remains largely ductile, and the presence of only minor quasi-cleavage features within a confined region further supports the alloy's low susceptibility to hydrogen embrittlement.

The quasi-cleavage fracture zone observed on the fracture surface is very limited in size and interspersed with traces of ductile dimples. Outside of the HAZs, the fracture surface exhibits predominant ductile dimple morphology, indicative of high ductility. Despite the presence of a localized hydrogen-affected quasi-cleavage zone on the fracture surface, L-PBF NASA HR-2 demonstrates substantial ductility, with fracture elongation values ranging from 34% to 36% following tensile testing in high-pressure hydrogen. Fractographic analysis clearly indicates that the interaction of external $GH_2$ with the tensile specimen is confined to regions near the surface. Hydrogen-induced surface cracks initiated from the specimen gauge surface and grew inward to depths of approximately 100–150 μm. Importantly, no evidence of intergranular fracture—often associated with severe HEE—was found on the fracture surface. This absence of brittle intergranular features further confirms the alloy's strong resistance to HEE.

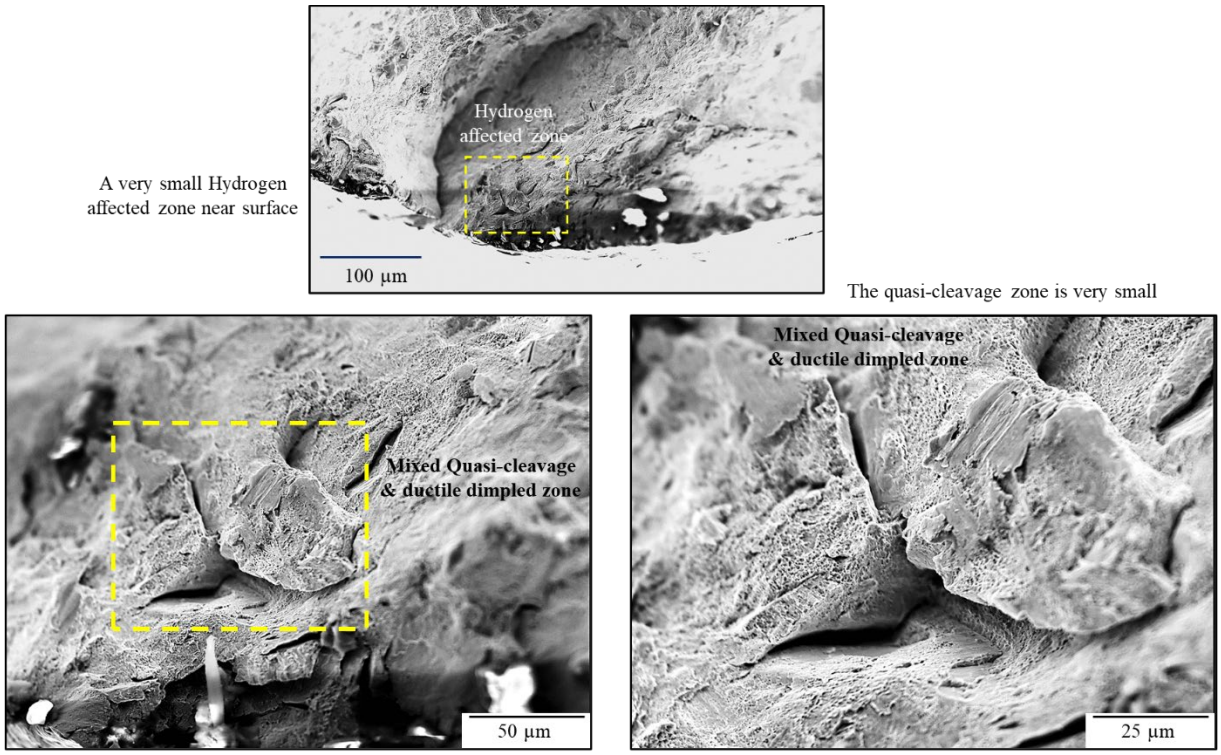


**Figure 35.** SEM fractography of a specimen tensile tested in hydrogen showing a very small hydrogen-affected zone on the specimen surface. The hydrogen-affected zone displays mixed quasi-cleavage fracture and ductile dimpled fracture.

## 5.0 Future Work (Hardware Manufacturing)

L-PBF NASA HR-2 has demonstrated excellent printability and resistance to HEE when processed using the EOS M100 system at MSFC. The development of L-PBF NASA HR-2 will continue and expand to a mid-sized EOS M290 system to enable the fabrication of larger samples and demonstration hardware.

Tensile properties of M290-built samples will be re-evaluated in both hydrogen and ambient air at various temperatures to compare the effects of transitioning from the M100 to the M290 platform. Additional critical mechanical property data, such as HCF and LCF, will be generated to verify that L-PBF NASA HR-2 can meet the fatigue life requirements for hydrogen-sensitive components in LREs.

Demonstration hardware will be fabricated using the M290 system to investigate the design limits for certain specific part features and explore the full potential of L-PBF NASA HR-2. The components to be demonstrated include turbine wheel, pump shaft, turbine rotators, turbine nozzle, turbine stator, and other pressure-loaded components used in the low-pressure fuel turbopump (LPFTP) of the RS-25 rocket engine, as shown in **Figure 36**. The project aims to demonstrate significant schedule and cost savings by targeting hydrogen-sensitive components that have complex shapes and fine features and are traditionally difficult to manufacture using forging or casting.

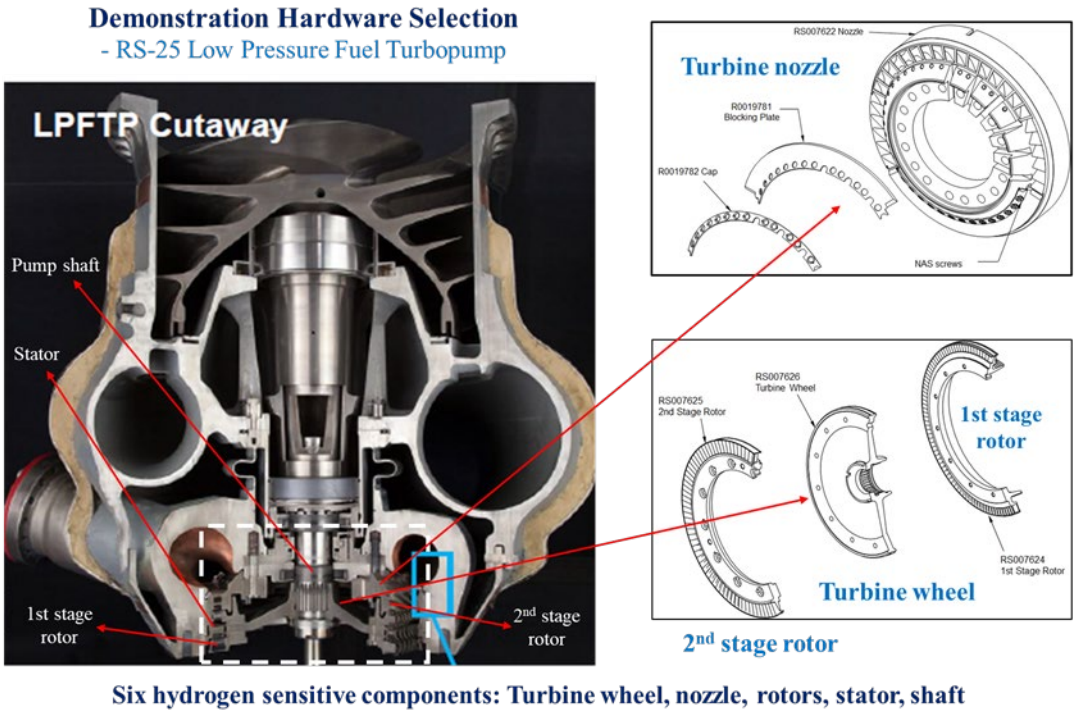


**Figure 36.** L-PBF NASA HR-2 will be demonstrated for several low-pressure fuel turbopump components that are used in high-pressure hydrogen environments for the RS-25 engine.

## 6.0 Conclusions

1. NASA HR-2 is a Ni-Fe-based superalloy specifically developed for AM and designed to meet the stringent demands of liquid rocket engine components that need resistance to HEE. The development of L-PBF NASA HR-2 has advanced through extensive process development, material characterization, and mechanical testing in both hydrogen and ambient air environments across a wide range of temperatures. NASA HR-2 components manufactured via the L-PBF process is defect free and has the desirable microstructure and tensile properties for hydrogen-sensitive aerospace applications.

2. The AM feasibility of NASA HR-2 alloy has been successfully demonstrated using the L-PBF technique. NASA HR-2 exhibits excellent printability and can be readily built with consistent quality using L-PBF. After heat treatment, its microstructure evolves well into a desirable highly recrystallized structure with very fine grain size. Its chemical composition was formulated to obtain an optimal balance of key performance attributes: HEE-resistance, printability, strength, ductility, oxidation resistance, and microstructure evolution after heat treatment. The optimized nominal composition is shown below:

| Alloy | Fe | Ni | Cr | Mo | W | Co | Ti | Al |
|---|---|---|---|---|---|---|---|---|
| L-PBF NASA HR-2 | 30.00 | 41.50 | 15.50 | 3.00 | 3.20 | 4.00 | 2.80 | 0.25 |

3. L-PBF NASA HR-2 has excellent resistance to HEE, maintaining high UTS and more than 34% fracture elongation after tensile testing in high-pressure hydrogen. The tensile data confirm that hydrogen has minimum influence on both tensile properties and fracture behavior of the alloy. Due to its outstanding HEE resistance, L-PBF NASA HR-2 is a promising option for many hydrogen-sensitive LRE components requiring high ductility and strength. Additionally, L-PBF NASA HR-2 also has excellent tensile properties in extremely cold environments. Its strength and ductility are significantly enhanced in cryogenic condition at –320 °F (in $LN_2$) and –423 °F (in $LH_2$).

4. NASA will continue to advance the development of L-PBF NASA HR-2 and demonstrate its potential of significant cost and schedule savings for complex aerospace components. Demonstration hardware will be fabricated to evaluate design limits and explore the full potential of L-PBF NASA HR-2. The components to be demonstrated include turbine wheel, pump shaft, turbine rotators, turbine nozzle, turbine stator, and other pressure-loaded components used in the LPFTP of the RS-25 rocket engine. Other critical mechanical property data such as HCF and LCF will be generated to ensure that the alloy can meet the fatigue life requirements for hydrogen-sensitive components in LREs.

## 7.0 References


1. Gradl, P.R., O.R. Mireles, C.C. Katsarelis, T.M. Smith, J.W. Sowards, A.M. Park, P.S. Chen, D.C Tinker, C.S. Protz, T.W. Teasley, D.L. Ellis, C.A. Kantzos. "Advancement of extreme environment additively manufactured alloys for next generation space propulsion applications," *Acta Astronautica* 211 pp. 483–497, 2023.

2. Chen, P.S., B. Panda, B.N. Bhat, "NASA HR-1, A New Hydrogen Resistant Fe-Ni Base Superalloy," in *Proc. of the Fifth International Conference on the Effect of Hydrogen on the Behavior of Materials,* A.W. Thompson and N.R. Moody (eds.), September 11–14, 1994, The Minerals, Metals and Materials Society, Moran, WY, pp. 1011–1020, 1996.

3. Chandler, W.T., "Hydrogen-Environment Embrittlement and Its Control in High Pressure Hydrogen/Oxygen Rocket System," *Advanced Earth-to-Orbit Propulsion Technology of NASA Conference Publication 2437*, no. 2, 1986.

4. Katsaleris, C.C., P.S. Chen, P.R. Gradl, C.S. Protz, D.L. Jones, L. Evans, "Additive Manufacturing of NASA HR-1 for Liquid Engine Component Applications", *JANNAF*, United States, December 2019.

5. Chen, P.S.; C.C. Katsarelis, W.M. Medders, P.R., Gradl, "Segregation Evolution and Diffusion of Titanium in DED NASA HR-1," NASA/TM 20210013649, May 2021.

6. Gradl, Paul R., Thomas W. Teasley, Christopher S. Protz, Colton C. Katsarelis, Po-Shou Chen, "Process Development and Hot-fire Testing of Additively Manufactured NASA HR-1 for Liquid Rocket Engine Applications," AIAA Propulsion and Energy Forum, 2021.

7. Chen, P.S., C.C. Katsarelis, W.M. Medders, P.R.Gradl, C.H. Su, "Development of Directed Energy Deposited NASA HR-1 to Optimize Properties for Liquid Rocket Engine Applications," NASA/TM 20230006075, April 2023.

8. Chen, P.S., M.D. Fullen, W.C. Watwood, B.L Rupp, W.M. Medders, C.C. Colton, P.R. Gradl, "Effects of Strain Rate and Surface Finish on Tensile Properties in High Pressure Hydrogen - A Case Study for LP-DED NASA HR-1," NASA/TM 20230008831, June 2023.

9. Brooks, J.A., R.W. Krenzer, "Progress Toward a More Weldable A-286," Welding Research Supplement, pp. 242–245, June 1974.

10. L-PBF JBK-75 Development, Internal Research, NASA Marshall Space Flight Center, AL.

11. Morinaga, M., N. Yukawa, H. Ezaki, H. Adachi, "Solid Solubilities in Transition-Metal-Based f.c.c. Alloys." *Philosophical Magazine* A, vol. 51, no. 2, pp. 223–246, doi:10.1080/01418610.1985.12069159, 1985.

12. Morinaga, M., Y. Murata, H. Yukawa, "Recent Progress in Molecular Orbital Approach to Alloy Design," 2004.

13. Morinaga, M., H. Yukawa, "Alloy Design with the Aid of Molecular Orbital Method." *Bulletin of Materials Science*, doi:10.1007/BF02747420, 1997.

14. Morinaga, M., N. Yukawa, H. Adachi, "Alloying Effect on the Electronic Structure of Ni3Al (γ′)," *Journal of the Physical Society of Japan*, vol. 53, no. 2, pp. 653–663, 1984.

15. Morinaga, M., N. Yukawa, H. Adachi, H. Ezaki, "Superalloys," E.A. Loria (ed), *The Minerals, Metals & Materials Society*, Warrendale, PA, pp. 523–532, 1984.

16. Morinaga, M., N. Yukawa, H. Adachi, "Alloying effect on the electronic structure of BCC Fe," *Journal of Physics F: Metal Physics*, vol. 15, no. 5, pp. 1071–1084, 1985.

17. Lee, J.A., "Effects of the Density of States on the Stacking Fault Energy And Hydrogen Embrittlement of Transition Metals And Alloys," *Effects of Hydrogen on Materials Proceedings of the International Hydrogen Conference*, B. Somerday, P. Sofronis, R. Jones, (eds.), pp. 678–685, 2008.

18. Katsuyuki, Toyoda, Fujita Hiroshi, Sawatari Hideaki, and Yoshida Kiyokazu, "Effect of Stacking Fault Energy on Recrystallization in Cold Worked FCC Crystals", *Transactions of the Japan Institute of Metals*, vol. 25, no. 5, pp. 339–347, 1984.

19. Ozbilen, Sedat, "Satellite formation mechanism in gas atomised powders," *Powder Metallurgy* 42(1), pp. 70–78, January 1999.

20. Keshavarzkermani, Ali, Reza Esmaeilizadeh, Usman Ali, Pablo D. Enrique, Yahya Mahmoodkhani, Norman Y. Zhou, Ali Bonakdar, Ehsan Toyserkani, "Controlling mechanical properties of additively manufactured hastelloy X by altering solidification pattern during laser powder-bed fusion," *Materials Science & Engineering* A 762, 138081, 2019.

21. Hibino, Shinya, Kazushige Fujimitsu, Makoto Azuma, Takuya Ishimoto, Takayoshi Nakano, "Effects of Recrystallization on Tensile Anisotropic Properties for IN738LC Fabricated by Laser Powder Bed Fusion," *Crystals*, 12, 842. https://doi.org/10.3390/cryst12060842, 2022.

22. David, S.A., J.A. Siefert, J.N. DuPont, P. Shingledecker, "Weldability and Weld Performance of Candidate Nickel Based Superalloys for Advanced Ultrasupercritical Fossil Power Plants Part I: Fundamentals," *Science and Technology of Welding and Joining*, vol. 20, no. 7, pp. 532–552, 2015.

23. Taghian, Mohammad, Mohammad Hossein Mosallanejad, Erika Lannunziata, Giovanni Del Greco, Luca Iuliano, Abdollah Saboori, "Laser powder bed fusion of metallic components: Latest progress in productivity, quality, and cost perspectives," *Journal of Materials Research and Technology* 27, pp. 6,484–6,500, 2023.

24. Obeidi, Muhannad Ahmed, "Metal additive manufacturing by laser-powder bed fusion: Guidelines for process optimization," *Results in Engineering* 15, 100473, 2022.

25. Yang, Kyung-Tae, Min-Kyeom Kim, Dongwon Kim, Jonghwan Suhr, "Investigation of laser powder bed fusion manufacturing and post-processing for surface quality of as-built 17-4PH stainless steel," *Surface & Coatings Technology* 422, 127492, 2021.

26. Evans, Rachel, Joy Gockel, "Surface Roughness Variation in Laser Powder Bed Fusion Additive Manufacturing," Solid Freeform Fabrication 2021: *Proceedings of the 32nd Annual International Solid Freeform Fabrication Symposium – An Additive Manufacturing Conference*.

27. Georgilas, Konstantinos, Raja H.U. Khan, and Mehmet E. Kartal," The influence of pulsed laser powder bed fusion process parameters on Inconel 718 material properties," *Materials Science & Engineering* A 769, 138527, 2020.

28. Kumar, Pankaj, Jano Farah, Javed Akram, Chong Teng, Jon Ginn, Mano Misra, "Influence of laser processing parameters on porosity in Inconel 718 during additive manufacturing," *The International Journal of Advanced Manufacturing Technology*, 103, pp. 1497–1507, 2019.

29. Robinson, Joseph Henry, Ian Robert Thomas Ashton, Eric Jones, Peter Fox, Chris Sutcliffe, "The effect of hatch angle rotation on parts manufactured using selective laser melting," *Rapid Prototyping Journal*, 25/2, pp. 289–298, Emerald Publishing Limited [ISSN 1355-2546], 2019.

30. Obeidi, Muhannad Ahmed, "Metal additive manufacturing by laser-powder bed fusion: Guidelines for process optimization," *Results in Engineering* 15, 100473, 2022.

31. Li, Lun, Sam Anand, "Hatch Pattern Optimization of Powder Bed Fusion Additive Manufacturing process for minimizing flatness error," *Procedia Manufacturing* 53, pp. 456–465, 2021.

32. Adomako, Nana Kwabena, Nima Haghdadi, Sophie Primig, "Electron and Laser-based additive manufacturing of Ni-based superalloys: A review of heterogeneities in microstructure and mechanical properties," *Materials & Design* 223, 111245, 2022.

33. Shaikh, Abdul Shaafi, "Development of a γ' Precipitation Hardening Ni-Base Superalloy for Additive Manufacturing," Department of Industrial and Materials Science, Chalmers University of Technology, Gothenburg, Sweden, https://www.researchgate.net/publication/326226200, 2018.

34. Sames, W.J, F.A. List, S. Pannala, R.R. Dehoff, S.S. Babu, "The metallurgy and processing science of metal additive manufacturing," *International Materials Reviews,* vol. 61, issue 5, 2016.

35. Adomako, Nana Kwabena, Nima Haghdadi, Sophie Primig, "Electron and laser-based additive manufacturing of Ni-based superalloys: A review of heterogeneities in microstructure and mechanical properties," *Materials & Design* 223, 111245, 2022.

36. Fencheng, L., L. Xin, Y. Gaolin, et al., "Recrystallization and its influence on microstructures and mechanical properties of laser solid formed nickel base superalloy Inconel 718," *Rare Metals*, vol. 30, no. 1, pp. 433–438, doi:10.1007/s12598-011-0319-0, March 2011.

37. Zhang, F, L.E. Levine, A.J. Allen, et al., "Effect of heat treatment on the microstructural evolution of a nickel-based superalloy additive-manufactured by laser powder bed fusion," *Acta Materialia*, vol. 152, pp. 200–214, June 2018.

38. Cao, J., F. Liu, X. Lin, et al., "Effect of overlap rate on recrystallization behaviors of Laser Solid Formed Inconel 718 superalloy," *Optics & Laser Technology*, vol. 45, pp. 228–235, February 2013.

39. Hibino, Shinya, Kazushige Fujimitsu, Makoto Azuma, Takuya Ishimoto, Takayoshi Nakano," Effects of Recrystallization on Tensile Anisotropic Properties for IN738LC Fabricated by Laser Powder Bed Fusion," *Crystals*, 12, 842, https://doi.org/10.3390/cryst12060842, 2022.

40. Keshavarzkermani, Ali, Reza Esmaeilizadeh, Usman Ali, Pablo D. Enrique, Yahya Mahmoodkhani, Norman Y. Zhou, Ali Bonakdar, Ehsan Toyserkani, "Controlling mechanical properties of additively manufactured Hastelloy X by altering solidification pattern during laser powder-bed fusion," *Materials Science & Engineering* A 762, 138081, 2019.

41. Weaver, Jordan S., Idan Rosenthal, "Understanding Anisotropic Tensile Properties of Laser Powder Bed Fusion Additive Metals: A Detailed Review of Select Examples," *NIST Advanced Manufacturing Series* 100-44. https://doi.org/10.6028/NIST.AMS.100-44.

42. Nandy, S., A.P. Sekhar, T. Kar, K.K. Ray, D. Das, "Influence of ageing on the low cycle fatigue behaviour of an Al–Mg–Si alloy," *Philosophical Magazine*, https://doi.org/10.1080/14786435.2017.1322729, 2017.

43. Saravanan, K., V.S.K. Chakravadhanula, S.K. Manwatkar, S.V.S. Narayana, P.R. Narayanan, "Dynamic Strain Aging and Embrittlement Behavior of IN718 During High-Temperature Deformation," *Metallurgical and Materials Transactions*, vol. 51A, pp. 5691–5703, November 2020.

44. Klopp, W. D., "A286," *Aerospace Structural Metals Handbook*, March 1987.

45. Ahmad, N., R. Ghiaasiaan, P.R. Gradl, S. Shao, N. Shamsae, "Revealing deformation mechanisms in additively manufactured Alloy 718: Cryogenic to elevated temperatures," *Materials Science & Engineering* A 849, 143528, 2022.

46. Poudel, A., P.R. Gradl, S. Shao, N. Shamsaei, Tensile deformation behavior of laser powder direct energy deposited Inconel 625: Cryogenic to elevated temperatures," *Materials Science & Engineering* A 889, 145826, 2024.

47. Nordström, J., R. Siriki, M. Calmunger, J. Moverare, G. Chai, "TWIP and Fracture Behavior in the Superalloy 625 at Room and Cryogenic Temperatures," *Procedia Structural Integrity* 23, pp. 457–462, 2019.

48. Anjaria, D., M. Heczko, R.L. Black, C. Bean, M.A. Reynolds, K. Zhang, D. Texier, V. Valle, M.J. Mills, D.C. Pagan, J.C. Stinville, "Plastic deformation delocalization at cryogenic temperatures in a nickel-based superalloy," *Acta Materialia* 276, 120106, 2024.

49. Wang, Y., J. He, P. Hu, C. Xiao, X. Wang, "Exceptional cryogenic tensile properties of K4169 superalloy by micro-grain casting process," *Materials & Design* 236, 112450, 2023.

50. Chalapathi, D., J. Nordström, R. Siriki, L. Lautrup, G. Chai, A. Kanjarla, "Deformation twinning and the role of stacking fault energy during cryogenic testing of Ni-based superalloy 625," *Materials Science & Engineering* A 898, 146404, 2024.

51. Nordström, J., Z. Dong, L. Lautrup, R. Siriki, L. Vitos, J. Moverare, M. Calmunger, G. Chai, "Temperature study of deformation twinning behavior in nickel-base Superalloy 625," *Materials Science & Engineering* A 907, 146628, 2024.

52. Lee, Jonathan A. "Hydrogen Embrittlement," NASA Technical Memorandum, 2016-218602.

53. Rao, G.S., Y. Yagodzinskyy, Z. Quea, P. Spätig, H.P. Seifert, "Study on hydrogen embrittlement and dynamic strain ageing on low-alloy reactor pressure vessel steels," *Journal of Nuclear Materials*, vol. 556, 153161, December 2021.

54. Nanninga, N., Y. Levy, E. Drexler, R. Condon, A. Stevenson, A. Slifka, "Tensile Behavior of Pipeline Steels in High Pressure Gaseous Hydrogen Environments," Materials Reliability Division. Boulder, CO: National Institute of Standards and Technology: 80305.